

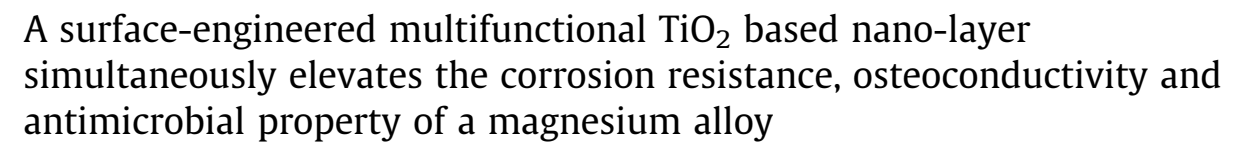
Contents lists available at ScienceDirect

Acta Biomaterialia

journal homepage: www.elsevier.com/locate/actabiomat



Full length article





Zhengjie Lin ^{a,b,c}, Shuilin Wu ^e, Xuanyong Liu ^f, Shi Qian ^{f,g}, Paul K. Chu ^h, Yufeng Zheng ⁱ, Kenneth M.C. Cheung ^b, Ying Zhao ^{d,**}, Kelvin W.K. Yeung ^{b,c,*}

- ^a College of Chemistry and Environmental Engineering, Shenzhen University, Shenzhen, PR China
- ^b Department of Orthopaedics and Traumatology, The University of Hong Kong, Hong Kong, China
- Shenzhen Key Laboratory for Innovative Technology in Orthopaedic Trauma, The University of Hong Kong Shenzhen Hospital, 1 Haiyuan 1st Road, Futian District, Shenzhen, China
- d Centre for Human Tissues and Organs Degeneration, Shenzhen Institutes of Advanced Technology, Chinese Academy of Sciences, Shenzhen 518055, China
- ^e School of Materials Science & Engineering, the Key Laboratory of Advanced Ceramics and Machining Technology by the Ministry of Education of China, Tianjin University, Tianjin 300072, China
- f State Key Laboratory of High Performance Ceramics and Superfine Microstructure, Shanghai Institute of Ceramics, Chinese Academy of Sciences, Shanghai 200050, China
- g Cixi Center of Biomaterials Surface Engineering, Shanghai Institute of Ceramics, Chinese Academy of Sciences, Ningbo, PR China
- h Department of Physics, Department of Materials Science and Engineering, City University of Hong Kong, Tat Chee Avenue, Kowloon, Hong Kong, China
- State Key Laboratory for Turbulence and Complex System and Department of Materials Science and Engineering, College of Engineering, Peking University, Beijing 100871, China

ARTICLE INFO

Article history: Received 12 June 2019 Received in revised form 12 August 2019 Accepted 6 September 2019 Available online 10 September 2019

Keywords:
Plasma ion immersion implantation
Anti-corrosion properties
Osteoconductivity
Antimicrobial activity
Magnesium implant

ABSTRACT

Magnesium biometals exhibit great potentials for orthopeadic applications owing to their biodegradability, bioactive effects and satisfactory mechanical properties. However, rapid corrosion of Mg implants in vivo combined with large amount of hydrogen gas evolution is harmful to bone healing process which seriously confines their clinical applications. Enlightened by the superior biocompatibility and corrosion resistance of passive titanium oxide layer automatically formed on titanium alloy, we employ the Ti and O dual plasma ion immersion implantation (PIII) technique to construct a multifunctional TiO₂ based nano-layer on ZK60 magnesium substrates for enhanced corrosion resistance, osteoconductivity and antimicrobial activity. The constructed nano-layer (TiO2/MgO) can effectively suppress degradation rate of ZK60 substrates in vitro and still maintain 94% implant volume after post-surgery eight weeks. In animal study, a large amount of bony tissue with increased bone mineral density and trabecular thickness is formed around the PIII treated group in post-operation eight weeks. Moreover, the newly formed bone in the PIII treated group is well mineralized and its mechanical property almost restores to the level of that of surrounding mature bone. Surprisingly, a remarkable killing ratio of 99.31% against S. aureus can be found on the PIII treated sample under ultra-violet (UV) irradiation which mainly attributes to the oxidative stress induced by the reactive oxygen species (ROS). We believe that this multifunctional TiO₂ based nano-layer not only controls the degradation of magnesium implant, but also regulates its implant-tobone integration effectively.

Statement of significance

Rapid corrosion of magnesium implants is the major issue for orthopaedic applications. Inspired by the biocompatibility and corrosion resistance of passive titanium oxide layer automatically formed on titanium alloy, we construct a multifunctional TiO₂/MgO nanolayer on magnesium substrates to simultaneously achieve superior corrosion resistance, satisfactory osteoconductivity in rat intramedullary bone defect model and excellent antimicrobial activity against *S. aureus* under UV irradiation. The current findings suggest that the specific TiO₂/MgO nano-layer on magnesium surface can achieve the three objectives aforementioned and we believe this study can demonstrate the potential of biodegradable metals for future clinical applications.

© 2019 Acta Materialia Inc. Published by Elsevier Ltd. All rights reserved.

^{*} Corresponding author. Department of Orthopaedics and Traumatology, The University of Hong Kong, Hong Kong, China (K.W.K. Yeung).

^{**} Corresponding author. Centre for Human Tissues and Organs Degeneration, Shenzhen Institutes of Advanced Technology, Chinese Academy of Sciences, China (Ying Zhao). E-mail addresses: yingzhao@126.com (Y. Zhao), wkkyeung@hku.hk (K.W.K. Yeung).

1. Introduction

Currently used stainless steel, cobalt and titanium based alloys in orthopaedic surgeries still present few shortcomings like biological inertia, stress shielding effects and requirement of secondary surgical removal upon bone healing [1]. Hence, a new initiative to design the next generation of biometal for orthopaedics has been considered in terms of appropriate biodegradability, suitable mechanical properties, and excellent biocompatibility. Biodegradable magnesium alloy is an attractive candidate due to human bone-like mechanical strength [2–4], where general biodegradable polymers do not possess [5]. This mechanical advantage may effectively reduce post-operative stress shielding effects in bone fracture fixation [6]. The implant made of magnesium alloy can degrade gradually in vivo so as to avoid secondary surgery for implant removal [7]. Also, when the degradation rate of magnesium alloy can be controlled properly, it exhibits improved biocompatibility and bone regeneration capability because of the upregulated adhesion, proliferation and differentiation of osteoblast and bone mesenchymal stem cells (BMSCs) induced by magnesium ions released [8-10]. However, despite of all these advantages, in vivo rapid corrosion found on general magnesium alloys is the major drawback. Indeed, magnesium is very active due to low standard electrode potential (-2.372 V) [11], galvanic corrosion easily occurs on this biometal when it is under physiological condition containing loads of chloride ions [12]. Moreover, rapid corrosion results in excessive hydrogen evolution and loss of mechanical integrity before bone fracture has completely repaired [13-15].

Therefore, many attempts such as surface treatment and addition alloying have been considered to enhance its corrosion resistance and mechanical strength upon degradation. For instance, various surface modifications such as chemical conversion [16], dip coating [2], micro-arc oxidation [17], sol-gel [18], and electrochemical deposition [19] have been employed to design functional protective coatings in order to enhance the corrosion property of magnesium alloys. Although various kinds of coatings have been reported to successfully enhance the corrosion resistance of magnesium implants in vitro and vivo [20–23], the protective coatings prepared by those methods usually present poor interfacial bonding and then result to delamination from Mg substrate, which may accelerate the corrosion of this biometal in vivo. As compared with the traditional surface treatment methods, plasma ion immersion implantation (PIII) [24] is a relatively versatile method to establish a functional layer on material surface which can be utilized in various applications like solar cells, semiconductor processing, film transistors corrosion protection and biomedical engineering. One of advantages of this technique is able to construct a nanolayer on material surface without an abrupt interface that prevents coating delamination from surface. Additionally, it only alters material surface property, while bulk mechanical properties remain unchanged [25]. Jamesh et al [26,27] has demonstrated that the corrosion current density (i_{corr}) magnitudes of ZrO₂ and ZrN based nanolayers on magnesium alloys treated by dual zirconium & oxygen PIII or zirconium & nitrogen PIII exhibit 37-fold and 12-fold decrease in simulated body fluid, respectively. Zhao et al [28] also employed zirconium & oxygen PIII technique to modify the surface of Mg based alloys in order to elevate their corrosion resistance and cytocompatibility in vitro.

As inspired by the superior anti-corrosion property and biocompatibility of passive titanium oxide (TiO_2) layer on titanium surface [29–31], we have constructed a specific TiO_2 based nanolayer on ZK60 magnesium surface by using titanium and oxygen dual PIII technique to regulate its degradation and bone-implant interface integration. The present study aims to systemically investigate

the degradation behavior of untreated and PIII treated ZK60 magnesium samples with the use of various solutions under dynamic corrosion and static corrosion conditions. The *in vitro* and *vivo* biological responses such as cell adhesion, viability, proliferation and osteogenic differentiation are also included. In addition, excellent osseointegration and bacteria disinfection are both required since implant instability and later stage loosening may adverse the bone remodeling process while microbial infection (mainly *Staphylococcus aureus*) initiates or accelerates the implant failure chances [32]. Hence, the antimicrobial activity of PIII-treated samples against *Staphylococcus aureus* and its underlying mechanism have been extensively characterized as well.

2. Materials and methods

2.1. Construction and characterization of TiO₂ based nano-layer

The as-cast ZK60 ingot (nominal composition: Mg-6 wt%Zn-0.5 wt% Zr; Jiaozuo Anxin Magnesium Alloys Scientific Technology Co., Ltd., China) was used as substrates and cut into cubes (size: $10 \times 10 \times 5 \text{ mm}^3$; in vitro study) and rods (size: $\varphi 2 \times 6 \text{ mm}^3$; in vivo study) by a linear cutting machine. The chemical composition of ZK60 alloy measured by energy dispersive spectrum was listed in Table 1. Before the experiments, ZK60 cubes or rods were grinded with 200, 400, 800 and 1200 grit silicon carbide papers, followed by ultrasonically cleaning in 95% ethanol for 15 min and being dried in nitrogen gas respectively. Afterwards, the ZK60 substrates were subjected to titanium plasms ion immersion implantation (PIII) by a HEMII-80 ion implanter (Plasma Technology Ltd, Hong Kong, China). The substrates were implanted by a titanium cathodic arc source for 2 h under working voltage of 25 kV and base pressure of 1.5×10^{-3} Pa. Then, ZK60 samples were further treated by oxygen PIII (radio frequency power:1000 W; pulse width: 100 µs; pulse frequency: 100 Hz) under a GPI-100 ion implanter (Plasma Technology Ltd, Hong Kong, China) at 30 kV for 3 h. During the implantation process, oxygen gas was continually delivered to the ion implanter chamber with a flow rate of 30 sccm and the base pressure was maintained at 8.0×10^{-2} Pa. After Ti and O dual PIII, the TiO₂ based nano-layer was constructed on the surface of ZK60 substrates and the Ti and O dual PIII treated ZK60 samples were denoted as PIII treated ZK60.

The transmission electron microscope (TEM; FEI Tecnai G2 20 S; EMU, the University of Hong Kong) was conducted to investigate the morphology of cross-sectional constructed TiO₂ nanolayer with the aid of focus ion beam (FIB) technique for sample preparation (Figure S1, Supporting information). In brief, the tungsten layer was deposited on the sample to protect the surface from gallium ion bombardment. Afterwards, the sample was ion milled by the FEI Quanta 200 3D machine (EMU, the University of Hong Kong) at 30 KV for 3 h and welded on the top of microprobe. The bright TEM images of the cross-sectional nanolayer were observed at 100 KV, while the Energy Dispersive Spectrometer (EDS) mapping analysis was conducted to detect the distributions of titanium, magnesium and oxygen elements in the nanolayer. Atomic force microscopy (AFM; Park Scientific Instruments) was employed to characterize the surface topography and roughness of untreated and PIII treated ZK60 samples.

The chemical states and depth profiles of TiO_2 based nano-layer on ZK60 substrates were investigated by X-ray photoelectron spectroscopy (XPS; Physical Electronics PHI 5802) under Al K α irradiation. The sputtering rate was estimated to be about 10.15 nm min⁻¹ according to sputtering a standard the SiO_2 sample as reference under the same condition. Phase and components of untreated and PIII treated ZK60 samples were analyzed by thin film X-ray diffraction (XRD; Rigaku Ultima IV, Japan) by using Cu-

Table 1
The nominal and chemical compositions of ZK60 magnesium alloys (wt%).

Nomina	al composit	ion	Chemical composition		
Mg	Zn	Zr	Mg	Zn	Zr
Bal.	6	0.5	Bal.	5.85 ± 0.17	0.47 ± 0.05

Kα radiation (λ = 1.541 Å;2 θ = 5°-90°). Diffraction patterns of each sample were identified with reference to JCPDS database. The surface hardness and modulus of samples before and after implantation were analyzed by a nano-indenter (Nano Indenter XP, MTS System Corporation, USA). The hydrophilicity of untreated and PIII treated ZK60 was evaluated by water contact angle assessment under the contact angle goniometer (Model 200, Rame-Hart, USA).

2.2. Corrosion behavior in vitro

Electrochemical tests were carried out by an electrochemical workstation (Zennium; Zahner; Germany) with three-electrode system. The saturated calomel electrode (SCE) was reference electrode while a platinum rod and sample served as the counter electrode and working electrode respectively. The three-electrode system was immersed in both simulated body fluid (SBF) and Dulbecco's modified Eagle's medium (DMEM) solutions at 37 °C. The SBF solution (pH 7.40) was as-prepared at 37 °C based on the standard protocol [28] containing the following ion concentrations: 142.0Na⁺, 2.5 Ca²⁺,1.5 Mg²⁺, 5.0 K⁺, 147.8 Cl⁻,1.0 HPO₄²⁻, 4.2 HCO_{3}^{-} , and 0.5 mM SO_{4}^{2} . The polarization curves were acquired by scanning the open circuit potential (OCP) with a rate of 1 mV s⁻¹ ranging from -300 mV to 600 mV. After stabilization in the SBF and DMEM solutions for 5 min, 10 mV sinusoidal perturbing signal was chosen as OCP and electrochemical impedance spectroscopy (EIS) was conducted on the frequency between 100 kHz and 100 mHz.

For investigation on static corrosion behavior, immersion tests were performed on the untreated and PIII treated ZK60 samples at 37 °C after soaking in SBF and DMEM solutions for 1, 3 and 7 days. In brief, samples were incubated with 10 mL both SBF and DMEM solutions at 37 °C to monitor magnesium ion release, pH value and weight loss of ZK60 substrates. The concentration of magnesium ions in each sample was examined by inductively-coupled plasma optical emission spectrometry (ICP-OES; Perkin Elmer; Optima 2100DV; USA) and a pH meter was used to measure the pH change. As for weight loss assessment, the soaked sample was rinsed with chromic acid (200 g L^{-1} CrO $_3^+$ and 10 g L^{-1} AgNO $_3$) to remove corrosion products on the surface and dried overnight for weight assessment. The surface morphology and components of samples in 3 and 7 days SBF immersion were analyzed by scanning electron microscopy (SEM, Hitachi S-3400N, Japan).

2.3. Cyto-compatibility in vitro

2.3.1. Cell culture

MC3T3-E1 mouse pre-osteoblasts were cultured in the DMEM solutions including 10% fetal bovine serum (FBS, Gbico, USA), 100 U ml $^{-1}$ penicillin and 100 μg ml $^{-1}$ streptomycin at 37 °C under the incubator with 5% CO $_2$ humidified atmosphere. Cell passages of MC3T3-E1 pre-osteoblasts occurred when they proliferated to more than 80–90% confluence. The fourth passage of cells were used in the experiments.

2.3.2. Cell adhesion

Prior to the cell studies, both untreated and PIII treated ZK60 samples were sterilized with 70% ethanol for 0.5 h and then rinsed

with phosphate-buffered saline (PBS) for three times. Then, MC3T3-E1 pre-osteoblasts with a density of 1.4×10^4 cells cm⁻² were seeded on the surface of specimens in a 24-well plate and incubated at 37 °C for 1 and 3 days with 5% CO₂ humidified atmosphere. The cells on the surface were rinsed with PBS for three times and fixed with 4% Paraformaldehyde solution for 15 min. The nuclei and cytoskeleton F-actin protein was stained with Hoechst 33342 (Sigma) and phalloidin-fluorescein isothiocyanate (Sigma) respectively. The cell image was captured by a fluorescence microscope (Sony DKS-ST5, Japan).

2.3.3. Cell proliferation

To evaluate cyto-toxicity of untreated and PIII treated ZK60 samples, the cell proliferation was analyzed by the 5-Bromo-2deoxyUridine (Brdu) incorporation assay. Similarly, MC3T3-E1 pre-osteoblasts at a density of 1.4×10^4 cells cm⁻² were cocultured with untreated and PIII treated ZK60 samples in the incubator at 37 °C under 5% CO₂ humidified atmosphere. At each time point (day 1 and 3), MC3T3-E1 pre-osteoblasts were rinsed with PBS (1x) three times and a ELISA Brdu kit (Roche, USA) was employed to quantify cell proliferations based on the recommended protocol. Firstly, 100 µM Brdu labeling solution was added to label cells. After 2 h incubation, cells were fixed with 4% Paraformaldehyde solution for 0.5 h followed by addition of the anti-Brdu-POD working solution. Then, substrate solution was added and incubated until color development was sufficient for photometric detection. 1 M H₂SO₄ was used to stop the reaction and absorbance was measured by a micro-plate spectrophotometer (Thermo Scientific, USA) at 450 nm with 690 nm for reference.

2.3.4. Cell differentiation and osteogenic expressions

The alkaline phosphatase (ALP) activity was adopted for characterization of osteogenic differentiation. 1.4×10^4 cells cm⁻² MC3T3-E1 pre-osteoblasts were incubated on the untreated and PIII treated ZK60 samples in the 24-well plate at 37 °C for 72 h. Afterwards. The DMEM was refreshed every two days with the differentiation DMEM which contained 50 uL ml⁻¹ ascorbic acid (Sigphosphate (Sigma) and ma).10 mM B-glycerol dexamethasone (Sigma). After 3,7 and 14 days culturing, MC3T3-E1 pre-osteoblasts were rinsed with PBS (1x) three times and lysed with the 0.1% Triton X-100 (Sigma, USA) solution at 4 for 30 min. The cell lysates were centrifugated by 574 g centrifugation at 4 °C for 10 min. 10 µL supernatant was transferred into a 96-well plate followed by addition of working reagent in the ALP reagents kit (Stanbio, USA). The ALP activity was determined by a colorimetric assay in which the formed rate of 4-nitrophenyl phosphate (4-NPP) was proportional to ALP activity. The absorbance per minute was measured by the micro-plate spectrophotometer (Thermo Scientific, USA) at 405 nm and ALP activity of MC3T3-E1 preosteoblasts was normalized to the total protein level via a Bio-Rad Protein Assay (Bio-Rad, USA).

To further evaluate osteogenic expression levels of MC3T3-E1 pre-osteoblasts cultured with samples, the RT-PCR assay was carried out and primers of four related bone markers like alkaline phosphatase (ALP), osteopontin (OPN), type collagen I (Col I), runt-related transcription factor 2 (RUNX2) and house-keeping geneglyceraldehyde-3-phosphate dehydrogenase (GAPDH) were used in our previous study [33]. 5×10^4 cells/well were cultured in the 6-well plate at 37 °C with 5% CO2 overnight. From day 4, $50~\mu L~mL^{-1}$ ascorbic acid, 10~mM β -glycerol phosphate and 10~nM dexamethasone were added and the conditioned DMEM were refreshed for every two days. At each time point, MC3T3-E1 pre-osteoblasts were rinsed with PBS three times and lysed by a Trizol reagent (Invitrogen, USA) followed by extraction of the total RNA into the upper aqueous phase by chloroform. Then the upper aqueous phase containing total RNA was transferred into a new

1.5 mL RNase-free centrifuge tube with addition of equal volume of isopropanol to precipitate the total RNA. 80% ethanol solution was used to rinse as-received RNA precipitates and the diethypyrocarbonate (DEPC)-treated RNase-free ddH2O was added to dissolve the RNA precipitates. A nano-drop 1000 spectrophometer (Thermo Scientific, USA) was employed to measure the concentration of isolated RNA. Afterwards, 1 µg isolated RNA was reverse-transcribed into the complementary DNA (cDNA) via a RevertAid First Strand cDNA Synthesis Kit (Thermo Scientific, USA). The reverse transcription reaction started at 42 °C for 1 h and terminated at 70 °C for 5 min. 5 μL cDNA template, 5 μL primers and 10 µL SYBR Green PCR Master Mix (Applied Biosystems, USA) were used for quantitative PCR reaction which was conducted on the Bio-Rad C1000 Touch™Thermal Cycler. 39 cycles of the reaction were set to amplify the signal for quantification and relative mRNA expressed levels of Col I. ALP. RUNX2 and OPN were normalized by GAPDH. Cells cultured with normal DMEM were set as the control group.

2.4. Antimicrobial assays

The antimicrobial assays including spread plate method and bacteria LIVE/DEAD staining were used to investigate antibacterial properties of Ti and ZK60 samples against Staphylococcus aureus (S. aureus; SF8300). Before the experiments, untreated and PIII treated ZK60 were irradiated by a 4 W ultraviolet lamp (UVA; Model UVGL-1; 365 nm) for 2 h. Untreated and PIII treated ZK60 samples under UV irradiation were named as untreated ZK60-UV and PIII treated ZK60-UV respectively while Mg samples without UV light were denoted as untreated and PIII treated ZK60. S. aureus were incubated on tryptic soy broth (TSB) plates overnight in the incubator at 37 °C. Then, inocula of S. aureus were gradually diluted 10-fold into 1.0×10^6 colony-forming units per mL (CFU mL⁻¹) of bacteria suspension. 200 μL bacteria suspension was added on the surface of each sample and incubated for 9 h. After stained by a LIVE/DEAD BacLight Viability Kit (Invitrogen) according to the recommended protocol, the bacteria were observed by confocal laser scanning microscopy (CLSM). The S. aureus growth on the surface of Ti and ZK60 samples after 2 h, 6 h and 12 h incubation at 37 °C was measured by the spread plate method. The control group was pure bacteria suspensions without addition of samples. Specifically, the adhered S. aureus on each the sample surface was added into 1 mL PBS and ultrasonic vibrated for 5 min. After removal of the supernatants, the remaining S. aureus was resuspended in 5 mL PBS to calculate the total amount of living bacteria via measuring absorbance of 600 nm by the micro-plate spectrophotometer. Then, bacteria suspensions were diluted and $100 \, \mu L$ supernatant was spread on the TSB plate for 24 h incubation at 37 °C. The viable counts (CFU) of S. aureus were examined according to the standard protocol (GB/T 4789.2, China). To investigate the underlying mechanism of antimicrobial activity, the pH values and detection of reactive oxygen species (ROS) production were conducted. In brief, 500 µL S. aureus suspensions at a concentration of $1.0 \times 10^6 \, \text{CFU} \, \text{mL}^{-1}$ were incubated on the sample surface for 6 and 12 h at 37 °C followed by measurement of pH values via a µe-pH meter (Model 60, Jenco, USA). For the ROS detection, 2,7-dichlorofluorescein diacetate (DCF-DA; Sigma) assay [34] was used to detect the level of intracellular oxidative stress. Before bacteria suspensions were incubated on the sample surface for 6 and 12 h, 10 mM DCF-DA was added into bacteria suspensions for labeling in a 37 °C incubator for 0.5 h. Total intracellular ROS amount was determined by a fluorescence microscope at excitation wavelength of 495 nm and emission wavelength of 525 nm respectively.

2.5. In vivo rat study

2.5.1. Surgical procedures

The surgical procedures and post-operative care protocol were licensed and strictly implemented according to the requirements of the Ethics Committee of the University of Hong Kong (CULATR NO.4086-16) and the Licensing Office of the Department of Health of the Hong Kong Government. Thirty female Sprague-Dawley (SD) rats (Ages:12-13 weeks old) with weight of 250-300 g were purchased from the Laboratory Animal Unit (the University of Hong Kong). Prior to the surgery, rats were anaesthetized via intraperitoneal injection of ketamine (67 mg kg^{-1}) and xylazine (6 mg kg⁻¹). After hair shaving, a Betadine solution was used for disinfection at surgical site and a hand driller was employed to intramedullary drill through the marrow cavity with implantation of untreated and PIII treated ZK60 rods (size: ω 2 × 6 mm³) on the right/left femur of rats (Fig. S2, Supporting information). Then the wound was sutured layer by layer and 1 mg kg⁻¹ terramycin and 0.5 kg mg⁻¹ ketoprofen were subcutaneously administered for antibiotic prophylactic and analgesic, respectively. The rats were euthanized at post-surgery four and eight weeks.

2.5.2. Micro-CT evaluation

New bone formation around the implanted untreated and PIII treated ZK60 rods was monitored by the micro-CT machine (SKY-SCAN 1076, Skyscan Company) at various post-operation time points (0, 1, 2, 4 and 8 weeks). At each time point, the percentage of new bone volume and implant volume, trabecular thickness (Tb, Th), and bone mineral density (BMD) of newly formed bony tissue were systemically analyzed by the CTAn software (Skyscan Company). The baseline on the percentual calculations was bone and implant volume at week 0. The percentages of new bone amount and implant volume indicated the change of new bone and implant volume at various time points by the following equations.

Change in bone volume

$$= \frac{\text{bone volume (week X) - bone volume (week 0)}}{\text{bone volume (week 0)}} \times 100\%$$

$$X = 1, 2, 4 \text{ and } 8$$
(1)

Change in implant volume

$$= \frac{implant\ volume\ (week\ X)}{implant\ volume\ (week\ 0)} \times 100\%\ \ X = 1,\ 2,\ 4\ and\ 8 \qquad (2)$$

The 3D models of new bone formation were reconstructed by the CTVol software (Skyscan Company). Tb, Th was estimated as the average thickness of all bony or tissue 3D structures in the region of newly formed bone in the CTAn software while the grey threshold in the CT densitometric analysis ranged 80 to 255 (–1000 to 9250 in Hounsfield units). The region of interest for quantitative calculation was a concentric cylinder (inner diameter/outer diameter: 2 mm/3 mm; 6 mm in depth).

2.5.3. Histological staining and Young's modulus of newly formed bone
The Giemsa solution (Giemsa(v):DI water(v) = 1:4, MERCK, Germany) was used to stain the newly formed bony tissue around the ZK60 implants. Briefly, the femur of rats euthanized at four and eight weeks were harvested and immersed into 10% buffer formalin solution for 72 h followed by the standard dehydration process of immersion in 70%, 95% and 100% ethanol solution respectively for each 72 h. Xylene was added as an intermedium for another 4 days immersion. Methyl metharylate (MMA) solutions at various stages (MMA I, MMA II, MMAIII and MMA IV) were adopted for embedding the samples for hard tissue cutting. The protocol has been described in our previous report [35]. Finally, the embedded

specimen was cut into slides (thickness: $50-70~\mu m$) by a microtome (EXAKT, Germany) and stained by the Giemsa solution at $57~^{\circ}C$ for 20 min. The images of stained femur slides were observed by an optical microscope. The stained slides were employed to measure Young's moduli of newly formed bone by a Nano Indenter (G200, MTS System Corporation, USA). During the tests, applied maximum load and drift rate were maintained at 10~mN and 1.2~mm s $^{-1}$, respectively. Six samples in each group were measured for statistical significance.

2.6. Statistical analysis

Five specimens in each group were measured at each time point including the *in vitro* and *vivo* tests while all *in vitro* cell tests were triplicated independently. The statistical analysis was determined by one-way analysis of variance via the SPSS software. The p value less than 0.05 was considered to be statistically significant.

3. Results

3.1. Surface characterizations

Fig. 1 depicted the morphology, chemical compositions, surface mechanical properties and hydrophilicity of the constructed TiO₂ nanolayer. Fig. 1a showed the cross-sectional TEM image of TiO₂ based nanolayer. Obviously, the nanolayer with a depth of about 70 nm was compactly constructed on the surface of ZK60 substrate. Furthermore, the EDS maps revealed that magnesium, titanium and oxygen elements were evenly distributed in the crosssectional TEM images of the constructed nano-layer. Moreover, the intensity of O signal was much higher than that of Ti and Mg signals, indicating that the nano-layer could be composed of titanium and magnesium-based oxide. The surface morphology in Fig. 1b-c demonstrated that obvious change of surface roughness was obtained after Ti and O dual PIII. The surface of PIII treated ZK60 was homogenous and smoother than untreated samples. The reason resulted to smooth surface was that large numbers of charges were easily accumulated on the "peaks" of the surface of ZK60 substrate during PIII process. Due to the bombardment of titanium and oxygen atoms, those peaks would be flattened. Therefore, the PIII-treated samples exhibited relatively smooth surface than that of untreated sample. It was beneficial to corrosion resistance since roughness topography of untreated samples could increase fluctuation of local electrode potential between peaks and valleys which promoted formation of microelectrodes locally and accelerated corrosion [36,37]. In addition, surface topography would alter the bioactivity of magnesium implants. The precipitation of calcium phosphate (CaP) was found to be highly correlated with surface topography and a rough surface was reported to directly proportioned to CaP formation. The smooth surface of PIII-treated sample wasn't conducive to the precipitation of CaP in which the osteoconductivity and bone-bonding capability of metallic implants would be compromised [38-40]. Moreover, rough surface was demonstrated to promote osteogenesis and bone-implant integration, while osteoclastic activity and formation was suppressed [41,42]. However, the smooth surface of PIIItreated ZK60 contributed to the elevated corrosion resistance, thereby manipulating a controllable release of magnesium ions to bone tissue microenvironment. These changes were favorable to accelerate the adhesion of osteoblastic cells thru the upregulation of β 1-, α 5 β 1-, and α 3 β 1-integrins receptors [43,44]. Furthermore, the tunable release of magnesium ions could promote insitu bone regeneration [45,46]. Therefore, the smooth surface created by the PIII technique had dual effects on bioactivity of magnesium substrates.

Fig. 1d-h revealed the XPS depth profile and correspondent high-resolution Mg 1s, Zr 3d, Ti 2p and O 1s XPS spectra of PIII treated ZK60 samples. A Ti and O rich layer was formed on the nearsurface of ZK60 substrates. The atom concentration of Ti increased to 37% then gradually dropped to near zero after 12 min sputtering while the atom concentration of O showed a downward trend from 54% to zero. Furthermore, the peak of Mg 1s spectra in Fig. 1e-g shifted from Mg^{2+} (1304.4 eV) to Mg^0 (1302.9 eV) while Ti 2p's peak changed from Ti⁴⁺ (458.6 eV), Ti²⁺ (457.4 eV) to Ti⁰ (454 eV). It implied that oxidized magnesium (Mg²⁺) and titanium (Ti⁴⁺, Ti²⁺) gradually converted into the metallic magnesium (Mg⁰) and titanium (Ti⁰) with increase of sputtering time. The oxidized magnesium (Mg²⁺) was easy to bind with O²⁻ to form MgO at binding energy (531.4 eV) whereas oxidized titanium (Ti⁴⁺, Ti²⁺) strongly bound with O^{2-} to form TiO_2 (529.8 eV), indicating that the main components of Ti and O rich nano-layer were calculated to be TiO₂ and MgO as shown in Fig. 1h. Furthermore, the XRD result in Fig. 1i revealed that compared to the same phase compositions of untreated ZK60 sample, the MgO and anatase TiO2 phase was detected from the near-surface of PIII treated ZK60, demonstrating that the constructed TiO₂ based nano-layer were mainly composed of MgO and anatase TiO2.

After Ti and O dual PIII, the surface mechanical properties were also disparate from ZK60 substrates. Fig. 1j-k exhibited hardness and modulus of untreated and PIII treated ZK60 samples. It was clearly seen that surface hardness and modulus was improved while the bulk substrates of two groups showed no significant difference, implying that PIII only adjusted the surface state without changing mechanical properties of substrates. The surface hydrophilicity of before and after ion implantation was evaluated by water contact angle assessments as depicted in Fig. 11. The contact angle of PIII treated ZK60 (71.6°) was slightly higher than the untreated sample (56.7°) which indicated the PIII treated surface was more hydrophobic owing to lower surface energy after ion implantation.

3.2. Corrosion behavior

The cyclic polarization curves and EIS spectra of untreated and PIII treated ZK60 samples in SBF and DMEM solutions were shown in Fig. 2. In cyclic polarization curves (Fig. 2a), the cathodic side represented cathodic hydrogen evolution while the anodic side was related to dissolution of magnesium substrates in the solution. In general, the forward scan stands for the polarization process of the non-corroded regions and the reverse scan represents the polarization of the corroded regions in the cyclic polarization curves [47]. Owing to the galvanic effects of magnesium alloys, the regions with relatively positive potential are protected, while the regions with relatively negative potential are subject to galvanic corrosion. For the untreated ZK60 sample immersed in SBF, the corrosion potential in forward scan (E_1^+) was higher than that of reverse scan (E₁), indicating that the corroded regions on ZK60 substrates functioning as the anode that tended to further erode. However, the non-corroded regions worked as the cathode to protect galvanic corrosion. This incident resulted in severe local pitting corrosion in the untreated ZK60 group. In contrast, the PIIItreated ZK60 group exhibited lower corrosion potential in forward scan than that of reverse scan $(E_2^+ < E_2^-)$. It revealed that the corroded regions worked as cathode to be protected by the noncorroded regions, while the non-corroded regions working as the anode would suffer from galvanic corrosion [48]. Therefore, the PIII-treated group was prone to be corroded under homogenous manner in electrochemical tests. The untreated and PIII-treated samples soaked in DMEM solutions exhibited the similar conditions. In addition, it was obvious that the corrosion potential (E⁺ and E⁻) in the polarization curves apparently enhanced while cor-

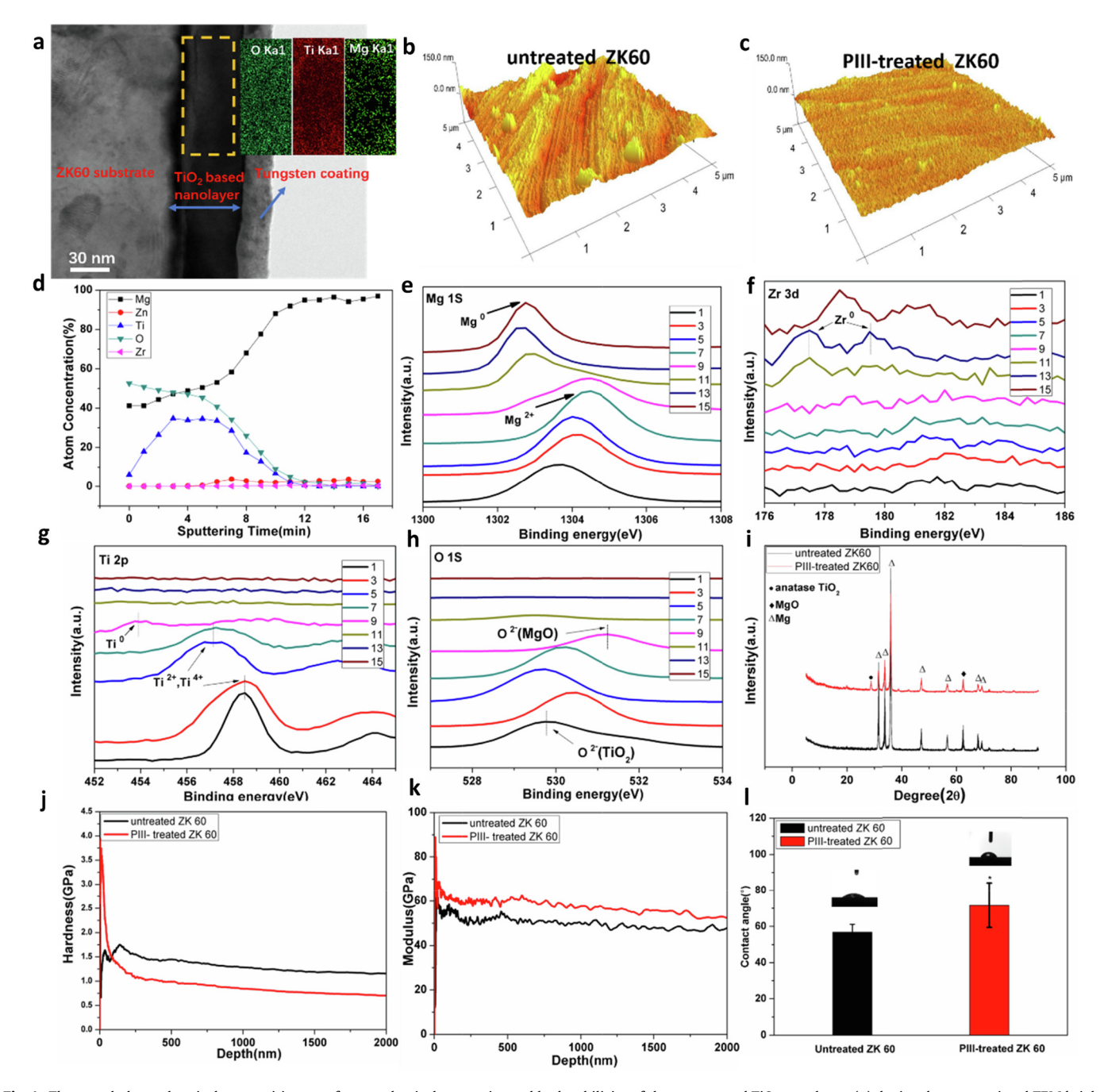


Fig. 1. The morphology, chemical compositions, surface mechanical properties and hydrophilicity of the constructed TiO₂ nanolayer. (a) depicted cross-sectional TEM bright image and corresponding EDS maps of PIII-treated ZK60 samples; (b-c) surface roughness of untreated and PIII-treated samples observed by AFM. (d-h) exhibited XPS depth profile and high-resolution XPS spectra acquired from PIII-treated ZK60 at various sputtering time (the numbers in the figures denoting the sputtering time); (i) depicted the thin XRD results while (j-l) revealed surface mechanical properties and water contact angle assessments of untreated and PIII-treated samples. *denotes significant difference between untreated ZK60 and PIII-treated ZK60 substrates (p < 0.05).

rosion current density (i⁺_{corr} and i⁻_{corr}) dropped in both SBF and DMEM solutions after Ti and O dual PIII. As one of the most important index of corrosion resistance, the lower i_{corr} of PIII treated ZK60 stood for lower corrosion rate in the solutions indicating suppressed degradation rate by the TiO₂ /MgO nano-layer. On the other hand, EIS spectra in the form of Nyquist Plots were depicted in Fig. 2b. Both high frequency and low frequency region exhibited capacitive loops in SBF and DMEM solutions. The capacitive loop in high frequency region corresponded to charge transfer whereas low frequency capacitive loop ascribed to mass transportation through the corrosion product layer [49]. The capacitive loop of both untreated and PIII treated samples in DMEM solution was

apparently larger than in SBF solution since protein in the DMEM could act as a inhibitor to block corrosion on magnesium substrates [50]. Furthermore, enlarged capacitive loops of PIII treated ZK60 samples was obviously seen and the capacitive arc in SBF and DMEM solutions exhibited approximately 14-fold and 6-fold increase respectively compared to untreated sample, which demonstrated better corrosion resistance due to the TiO₂ based nano-layer on the ZK60 surface.

Fig. 3 revealed corrosion behavior of samples soaking in SBF and DMEM solutions at 37 °C for 1, 3 and 7 days. The concentration of magnesium ion release, pH value and weight loss of substrates were measured to evaluate corrosion properties of specimens

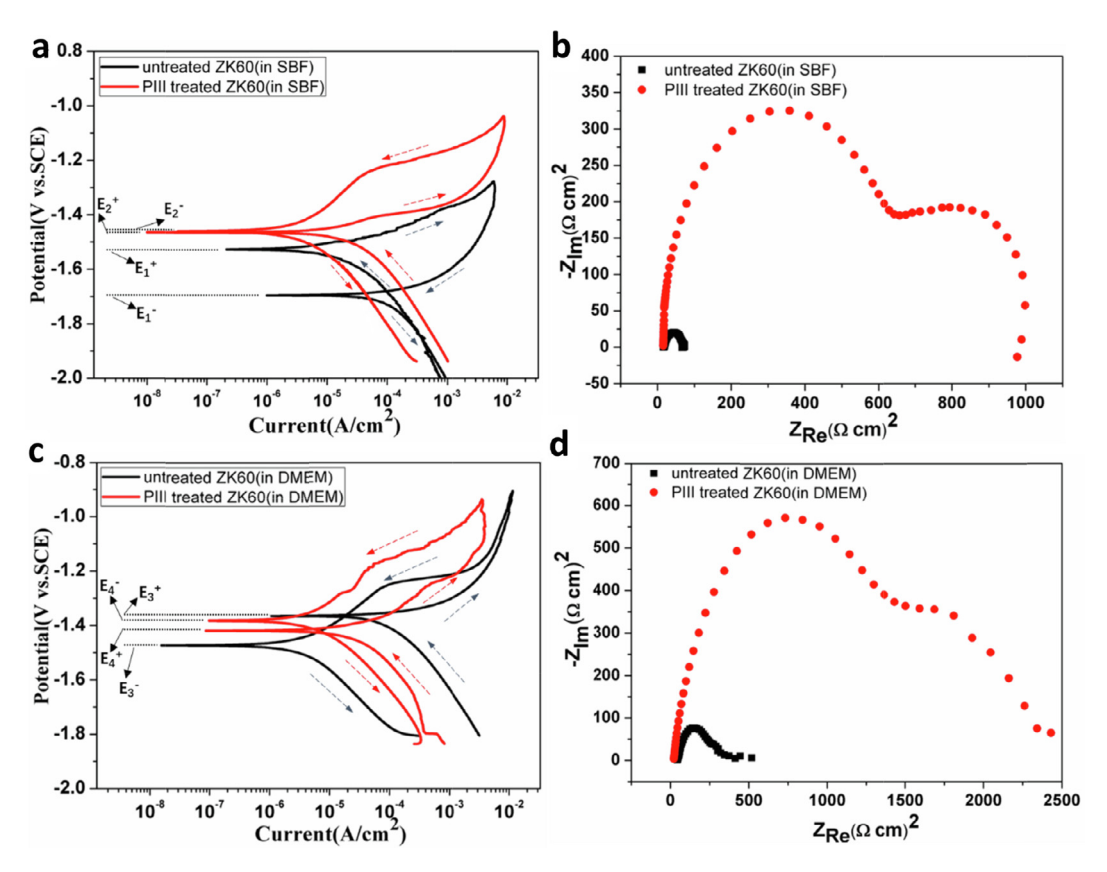


Fig. 2. Cyclic polarization curves and electrochemical impedance spectroscopy (EIS) of untreated ZK60 and PIII-treated ZK60 alloys immersed in (a)(b) SBF and (c)(d) DMEM at 37 °C.

under static corrosive conditions. Overall, for the PIII treated group, concentration of magnesium ion release, pH value and weight loss were lower than untreated group after 1, 3 and 7 days immersion. The concentrations of magnesium ions leached from PIII treated ZK60 in SBF and DMEM at day 3 were 210 ppm and 118 ppm respectively, which were significantly lower (p < 0.05) than untreated ZK60 (359 ppm and 157 ppm). Moreover, pH value and weight loss of PIII treated sample also significantly (p < 0.05) decreased as compared with untreated sample after 3 days soaking in both SBF and DMEM. All these results confirmed that under static corrosive conditions, TiO₂/MgO nano-layer on ZK60 substrate could appreciably suppress corrosion rate of ZK60 alloy, resulting in relatively reduced magnesium ion release and pH change. The surface morphology of samples after 3 and 7 days SBF immersion at 37 °C was shown in Fig. 4. It was clearly seen that big corrosive cracks with some small cracks were formed on the untreated surface whereas the PIII treated sample was still intact without obvious cracks on the surface at day 3 and 7. These cracks functioned as channels for intrusion of corrosive solution containing chloride ions which accelerated further corrosion of ZK60 substrates. In short, regardless of static and dynamic corrosive conditions, the TiO2 /MgO nano-layer acting as a corrosion-resistant layer could remarkably improve corrosion resistance of ZK60 substrates.

3.3. Cyto-compatibility in vitro

Fig. 5a depicted fluorescent images of MC3T3-E1 preosteoblasts adhesion on the untreated and PIII treated ZK60 at day 1 and 3. After incubated for one day, it was obvious that both untreated and PIII treated ZK60 samples exhibited no toxicity to pre-osteoblasts. The cells were well spread and the protein Factin of cytoskeleton was even flattened on the surface. Furthermore, as compared to the untreated group, an enhanced adhesion of MC3T3-E1 pre-osteoblasts could be observed on the PIII-treated group at day 3 due to the controlled release of magnesium ions. Similarly, referring to the cell proliferation assay, the amount of Brdu incorporation in the PIII treated ZK60 group (Fig. 5b) presented significantly 1.7-fold and 2.5-fold increase at day 1 and 3, respectively. It implied that the TiO2 /MgO nano-layer controlled magnesium ion release of ZK60 substrates in vitro which improved osteoblasts viability and proliferation. Moreover, the ALP protein expression of the PIII treated group portrayed in Fig. 5b was significantly 83% (p < 0.05) and 47% (p < 0.05) higher than the untreated control at day 7 and 14 respectively, indicating promoted preosteoblast differentiation owing to controllable magnesium ion delivery by the protective TiO2 /MgO nano-layer. Furthermore, with regards to osteogenic differentiation expression as shown in Fig. 5c, both osteogenic expressions of OPN and Col I in the PIIItreated ZK60 group exhibited 2-fold increase (p < 0.01) and 2.5fold increase (p < 0.001) at day 7 and 14 compared with untreated samples while the ALP osteogenic expression was statistically upregulated two (p < 0.01) and four times (p < 0.001) respectively. Additionally, remarkably higher (p < 0.05) expression of RUNX2 was obtained from the PIII-treated ZK60 samples after 7 and 14 days incubation. All these results demonstrated that with the aid of regulated magnesium ion release, enhanced osteoblastic activities of proliferation, differentiation and osteogenic expressions were achieved in the PIII-treated samples.

3.4. Antimicrobial activity

Fig. 6 revealed Live/Dead staining images of *S. aureus* suspensions on Ti, untreated ZK60, untreated ZK60 irradiated at UV light (untreated ZK60-UV), PIII treated ZK60 and PIII treated ZK60 irradiated

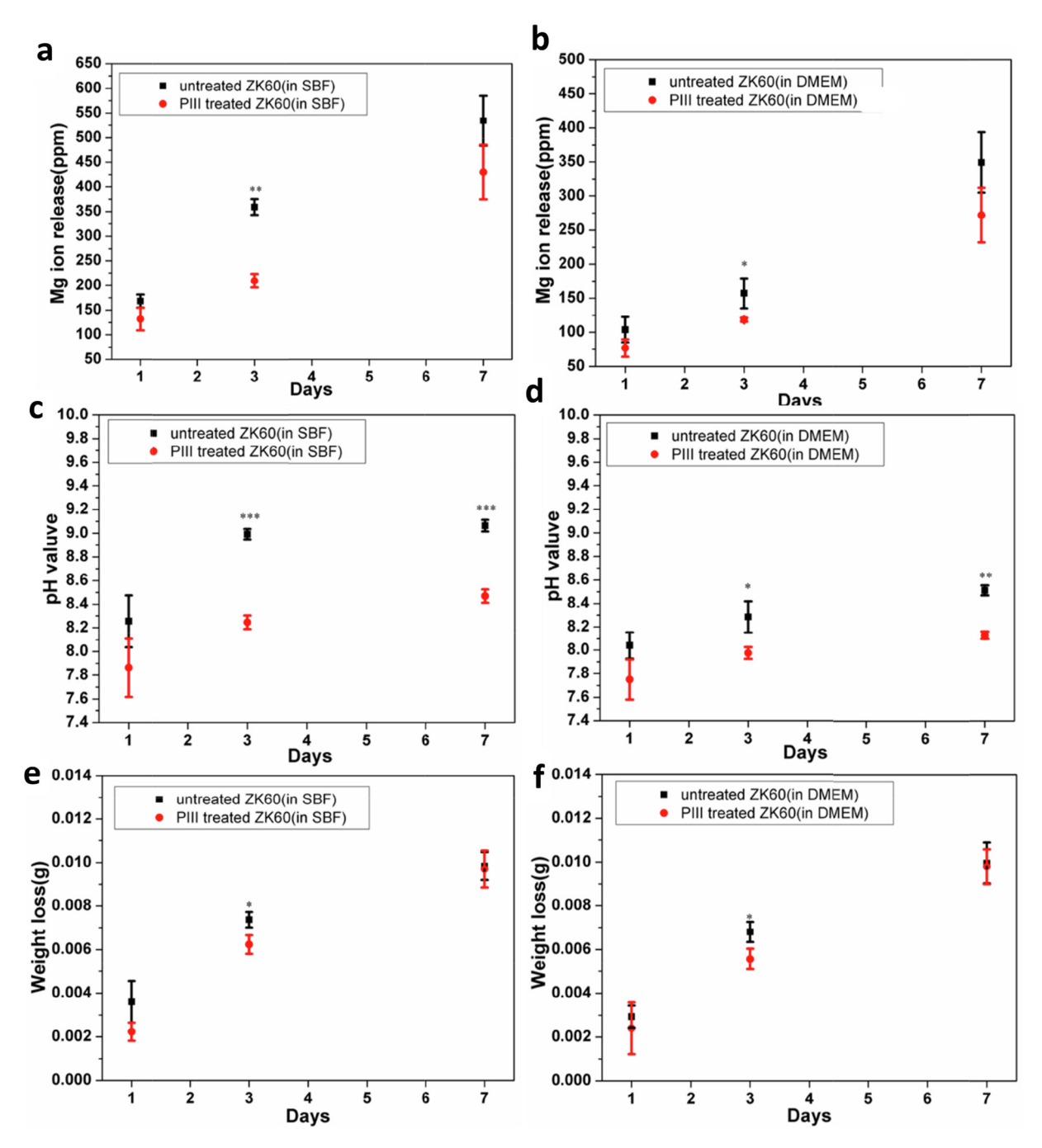


Fig. 3. Corrosion behavior of untreated ZK60 and PIII-treated ZK60 alloys immersed in SBF and DMEM at 37 °C for 1, 3 and 7 days. The corrosion behavior was characterized by (a)(d) Mg ion release, (b)(e) pH value and (c)(f) weight loss measurements. *denotes significant difference between untreated ZK60 and PIII-treated ZK60 alloys (p < 0.05).

ated at UV light (PIII treated ZK60-UV) samples for 9 h incubation. It was clearly seen that Ti group exhibited rare death of *S. aureus* on the surface while large amount of *S. aureus* was dead with few bacteria survival on the PIII treated ZK60-UV sample, implying superior antimicrobial properties of PIII treated ZK60-UV samples against *S. aureus*. As for other three groups, all untreated ZK60, untreated ZK60-UV and PIII treated ZK60 groups showed that most bacteria were still alive although few bacteria dead on the surface. Similarly, optical images of *S. aureus* cultured on TSB plates in Fig. 7a confirmed that the number of surviving *S. aureus* in the PIII treated ZK60-UV group was smallest among all the groups regardless of incubation for 2 h, 6 h and 12 h. Moreover, no obvious *S. aureus* colony on the TSB plates was formed in the PIII treated ZK60-UV sample after 6 h and 12 h incubation. Nevertheless, PIII treated ZK60 group pre-

sented a few viable *S. aureus* colonies remained on the TSB plates at 6 h and 12 h. Fig. 7b showed concentration of bacteria colonies in each group after 2 h, 6 h and 12 h incubation analyzed by spread plate method. Obviously, the concentration (CFU $\rm mL^{-1}$) of all magnesium-based groups and Ti group was remarkably lower (p < 0.001) than that of the control group while PIII treated ZK60-UV group exhibited significantly lower (p < 0.001) *S. aureus* colonies survival at 6 h and 12 h compared to the PIII treated ZK60-UV samples were 0.192 \times 10 5 CFU $\rm mL^{-1}$ and 0.096 \times 10 5 CFU $\rm mL^{-1}$ at 6 h and 12 h respectively, which were calculated to be 98.63% and 99.31% of antibacterial ratio against *S. aureus* normalized to the control group. To further investigate antimicrobial mechanism of PIII treated ZK60 samples irradiated at UV light, the pH value and ROS

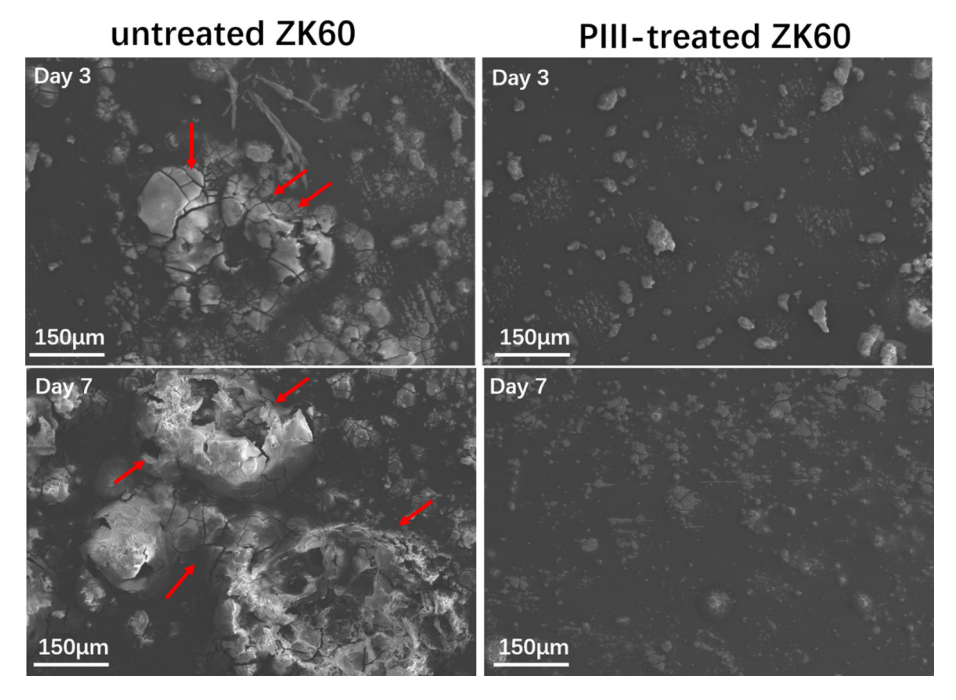


Fig. 4. SEM images of untreated ZK60 and PIII-treated ZK60 alloys immersion in SBF at 37 °C for 3 and 7 days. The surface of PIII treated ZK60 was still intact without visible microcracks at day 3 and 7 while untreated sample exhibited large numbers of microcracks on the surface.

production of bacteria suspensions on the surface were depicted in Fig. 7c-d. After 6 h and 12 h incubation, PIII treated ZK60-UV and PIII treated ZK60 groups showed almost the same pH values (approximately 8.70 and 8.90), which were apparently lower than that of untreated ZK60-UV and untreated ZK60 groups (about 9.70 and 10.0). Nevertheless, as for amount of ROS generation, PIII treated ZK60-UV groups presented appreciably 250% and 300% increase (p < 0.001) of ROS production in comparison with other four groups at 6 h and 12 h respectively. It meant that the antimicrobial activity of PIII treated ZK60-UV sample mainly ascribed to a surge of ROS generation other than pH change.

3.5. In vivo rat study

Fig. 8 depicted the micro-CT qualitative and quantitative evaluations of new bone tissue formed around untreated and PIII treated ZK60 rods at post-surgery various time points. Fig. 8a revealed micro-CT reconstruction images of the intercondylar fossa implanted with ZK60 rods and correspondent 3D reconstructed models at post-surgery 0, 1, 2, 4 and 8 weeks. For the untreated ZK60 group, significant inflammatory response occurred at postoperation week 2, leading to severe bone absorption surrounding the implant. Meanwhile, it could be clearly seen that rapid corrosion of untreated ZK60 rods appeared at week 8 and less amount of bony tissue remained in the site corrosion happened. In contrary, new formed bone tissues were observed progressively through monitored time points in the PIII treated ZK60 group and newly formed bone closely integrated with the implant. Quantitative characterizations of new bone formation around the ZK60 implants including percentage change of new bone volume, percentage change of implant volume, bone mineral density (BMD), and trabecular thickness (Tb. Th) were portraved in Fig. 8b. Bone volume of PIII treated ZK60 group showed a gradual upward from 10.5% to 116.3% while bone volume in the untreated ZK60 group dropped gradually from -22.1% to -54.8% and then increased to -33.1% at week 8, which indicated new bone volume was formed one-fold increase around PIII treated ZK60 rods and bone volume surrounding untreated ZK60 rods at week 8 reduced about 30% compared to that of week 0. At post-surgery 2, 4 and 8 weeks, all the bone volume was significantly higher (p < 0.001) than the untreated control. On the other hand, the untreated ZK60 rods degraded approximately 30% in Fig. 8b while the implant volume of PIII treated samples still retained 94% at week 8, implying that TiO_2/MgO nanolayer could retard rapid corrosion of ZK60 substrates *in vivo*. Moreover, all BMD, and Tb, Th in the PIII treated group presented statistically 75% (p < 0.05), and 43% (p < 0.01) increase respectively compared to the untreated control, demonstrating that better newly formed bone quality was achieved in the PIII treated samples.

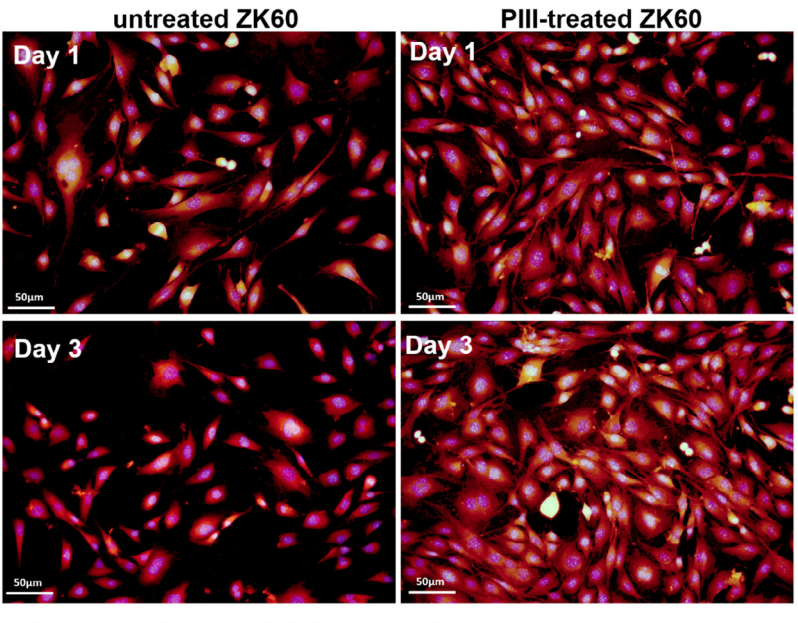
The optical images of Giemsa-stained bony tissue around the implants in Fig. 9a displayed that rarely bony tissue was observed around untreated ZK60 rod and the trabecular bone was brittle surrounded by large numbers of osteoclasts at week 4 and 8. Meanwhile, necrotic tissues combined with corrosion products (red circle in untreated group) owing to rapid degradation were deposited around the outer edge of implants. However, plenty of newly bony tissue with well mineralized structure was stimulated around the PIII treated rods. Moreover, newly formed bone tissue bond with implants compactly which exhibited excellent osteoconductivity of the PIII treated ZK60 rod. Fig. 9b showed Young's modulus of bone tissues in each group measured by the nanoindentation assay. The Young's moduli of newly formed bony tissue around untreated ZK60 implants was only 6.8 GPa after postsurgery eight weeks. In contrast, the Young's moduli in the PIII treated group exhibited to be 11.9 GPa, which was significantly higher (p < 0.001) than that of the untreated group. Normalized by the moduli of surrounding mature bone (13.0 GPa), the moduli of newly formed bone around the PIII treated sample could restore 91.5% mechanical property of surrounding mature bone while the untreated group only restored 52.3%. It implied that in terms of mechanical property, newly formed bone in the PIII treated group could almost reach the level of surrounding mature bone.

4. Discussion

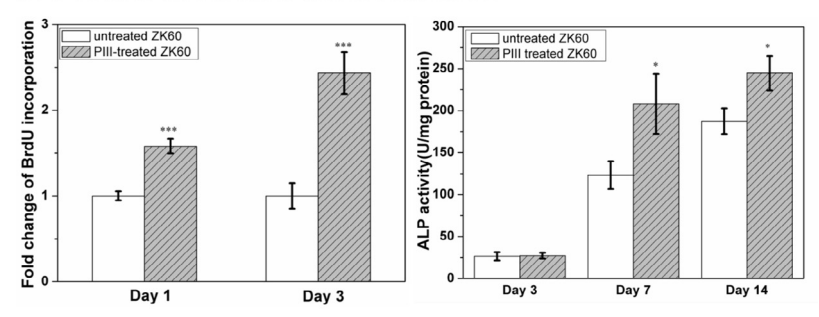
4.1. Anti-corrosion property of functionalized TiO₂/MgO nanolayer

Rapid corrosion of magnesium alloy is the major concern of applications in orthopaedic implants. It has been demonstrated

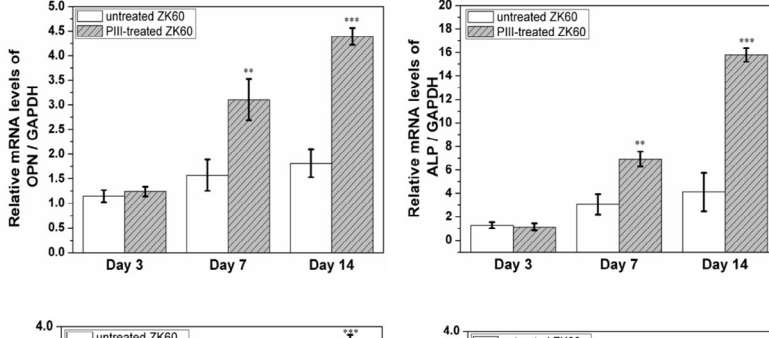
a. Cell attachment



b. Proliferation and differentiation



c. Osteogenic expression



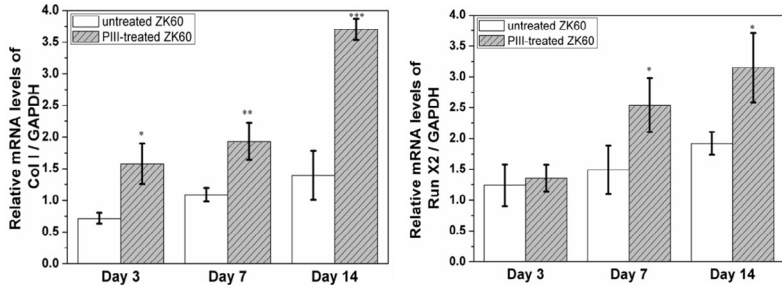


Fig. 5. The cyto-compatibility of MC3T3-E1 pre-osteoblasts on the untreated and PIII treated ZK60 groups *in vitro*. (a) depicted fluorescence images of MC3T3-E1 pre-osteoblasts cultured on the surface of untreated ZK60 and PIII treated ZK60 groups (incubation for 1 and 3 days). (b) showed fold change of the incorporation of BrdU and ALP activity assays of MC3T3-E1 pre-osteoblasts cultured with untreated and PIII treated ZK60 samples that immersed in DMEM at 37 °C while (c) presented osteogenic expression assessed by RT-PCR assay after incubation in DMEM at 37 °C on day 3, 7 and 14. The osteogenic expression was determined by relative mRNA expressed levels of alkaline phosphatase (ALP), osteopontin (OPN), type collagen I (Col I) and runt-related transcription factor 2 (RUNX2) normalized to the house-keeping gene glyceraldehyde-3-phosphate dehydrogenase (GAPDH). * denotes the significant difference between PIII-treated ZK60 alloy and untreated ZK60 alloy (p < 0.05); ***(p < 0.01); ***(p < 0.001).

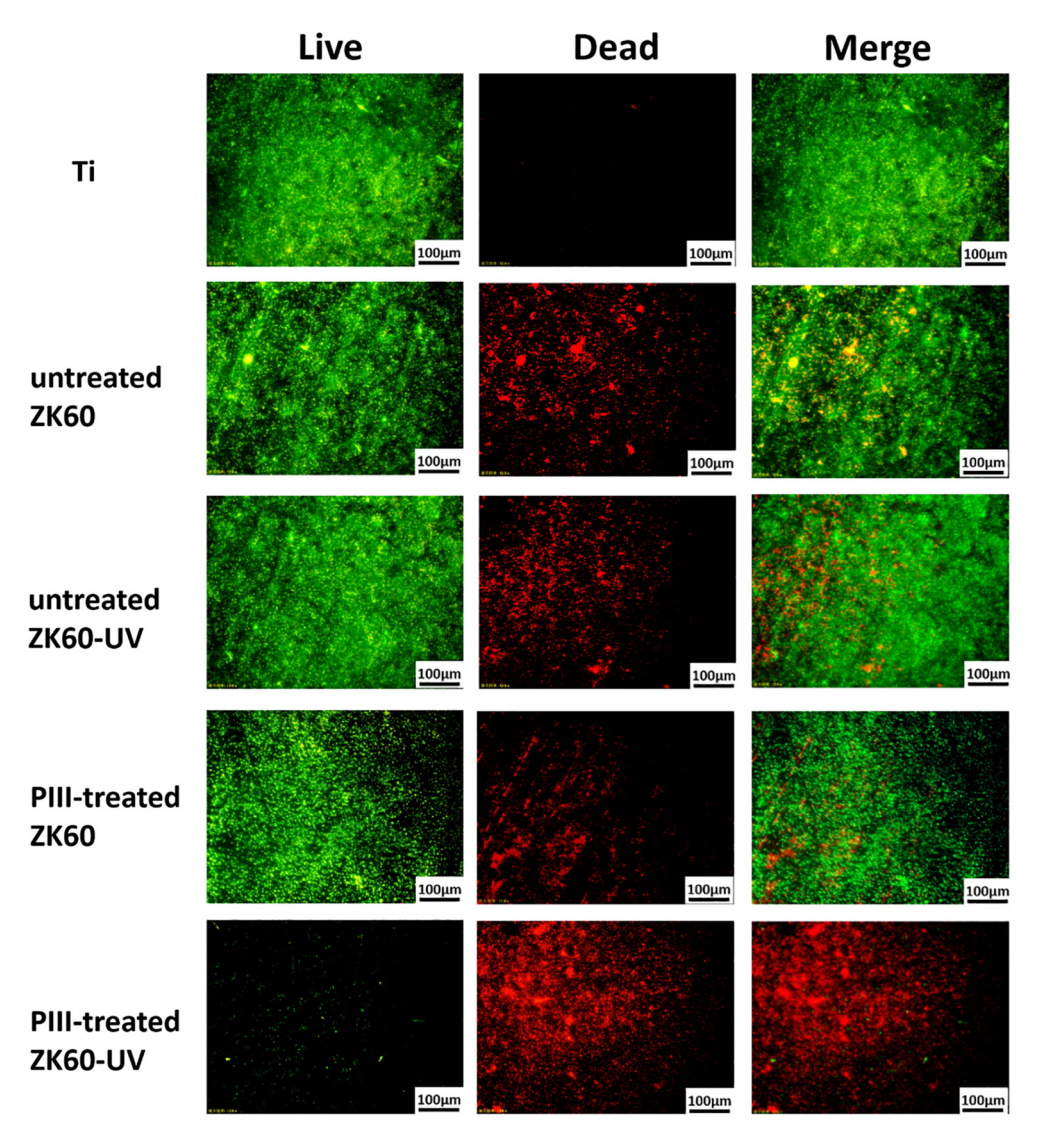


Fig. 6. Live/Dead fluorescence images of *S. aureus* suspensions on the surface of Ti, untreated ZK60, untreated ZK60-UV, PIII treated ZK60 and PIII treated ZK60-UV samples at 37 °C for 9 h incubation. The green color represented for living bacteria while the red color referred to dead bacteria. PIII treated ZK60-UV group showed large amount of dead *S. aureus* on the surface with few bacteria living indicating the excellent antimicrobial activity. (For interpretation of the references to color in this figure legend, the reader is referred to the web version of this article.)

that rapid degradation in vivo not only causes large amount of hydrogen evolution and alkalosis in the microenvironment which is detrimental to bone remodeling and healing process [51-53] but also leads to excessive magnesium ion delivery locally inhibiting human osteoblast differentiation [54] and disordering bone mineralization process [55,56]. It has been demonstrated that Mg²⁺ release at concentration higher than 5 mM inhibited osteogenic activity of human osteoblasts [54]. Therefore, it is an imperative issue to suppress degradation of magnesium-based implants. Through the plasma ion immersion implantation technique, we construct a TiO₂ based nanolayer (main components: TiO₂ and MgO) on the ZK60 alloys to protect Mg substrates from further corrosive attack. More importantly, the surface functionalized TiO₂/ MgO nanolayer can achieve three objectives simultaneously: enhanced corrosion resistance, osteogenic activities due to controlled release of Mg²⁺ and bacteria disinfection under a photocatalytic effect.

The results of corrosion behavior *in vitro* confirm that enhanced corrosion resistance of PIII treated ZK60 samples immersion in SBF and DMEM are achieved regardless of dynamic and static corrosive

conditions. To unveil the underlying mechanism, electrical equivalent circuits of EIS spectra (Fig. 2) in the SBF and DMEM solutions are drawn in Fig. 10. The different equivalent circuits reveal distinct corrosion behaviors of ZK60 samples in SBF and DMEM solutions which may attribute to the chemical compositions of solution. Proteins (e.g. albumin) contained in the DMEM solutions have been demonstrated to be able to change the corrosion rate of metallic implant via the surface diffusion and charge transfer process [57]. Furthermore, the presence of albumin in SBF solutions tends to form a blocking payer on the surface to suppress the corrosion reaction of magnesium alloys, leading to the discrepancy between the simulated equivalent circuits in SBF and DMEM solutions. In the simulated equivalent circuits, R_s stands for solution resistance between working and reference electrodes while R_f and R_t correspond to resistance of the corrosion product layer and the relevant charge transfer, respectively. Constant phase elements, CPE_f and CPE_{d1}, represent the capacitance of the corrosion product layer and double layer at the Mg substrate surface while L and R_1 equal to inductance and inductive resistance, respectively. Values of each component in the equivalent circuits calculated

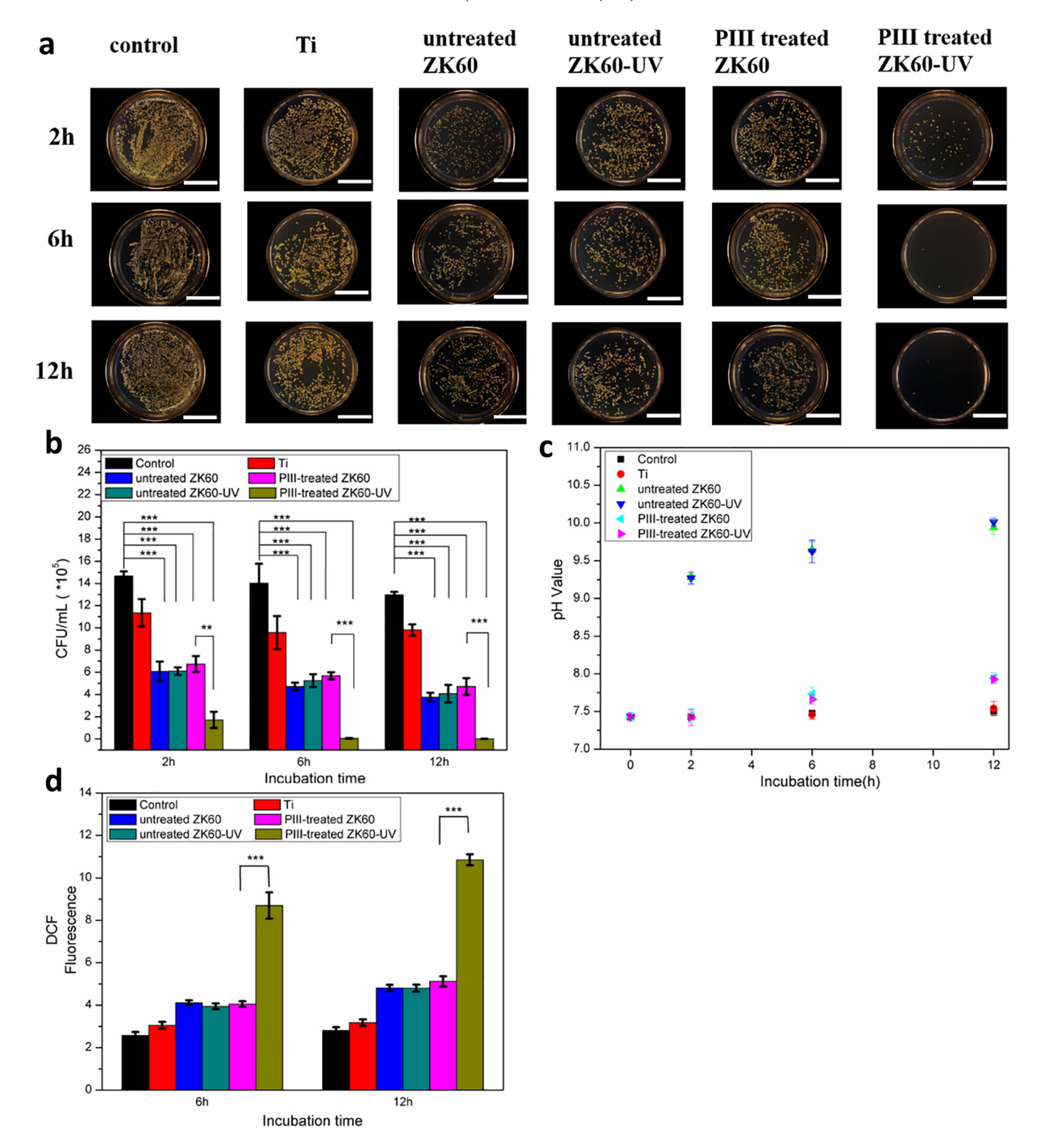


Fig. 7. Antimicrobial assay of Ti and ZK60 based groups against *S. aureus in vitro*. Fig. 7a and b revealed living bacteria counts (CFU ml $^{-1}$) of Ti and ZK60 based groups evaluated by the spread plate method after 2, 6 and 12 h incubation at 37 °C (scale bar: 3 cm). Fig. 7c and d showed pH value of *S. aureus* suspensions of each group and intracellular total ROS amount detected with 2,7-dichlorofluorescein diacetate (DCF-DA) assay. The control group was bacteria suspensions without addition of samples. ***denotes the significant difference between PIII treated ZK60 and PIII treated ZK60-UV groups (p < 0.001).

from the EIS spectra, corrosion current density and corrosion potentials of forward scan $(i_{corr}^+; E^+)$ and reverse scan $(i_{corr}^-; E^-)$ obtained from the polarization curves are all listed in Table 2. E^+ of PIII treated ZK60 samples in SBF and DMEM immersion are

-1.43 and -1.37 V/SCE, which exhibit 6.7% and 3.1% increase compared to the untreated samples. Additionally, i_{corr}^{\star} of PIII treated ZK60 samples drops 88.5% and 62.2% in the SBF and DMEM solutions, respectively. Both elevated E and descendant i_{corr} lead to pro-

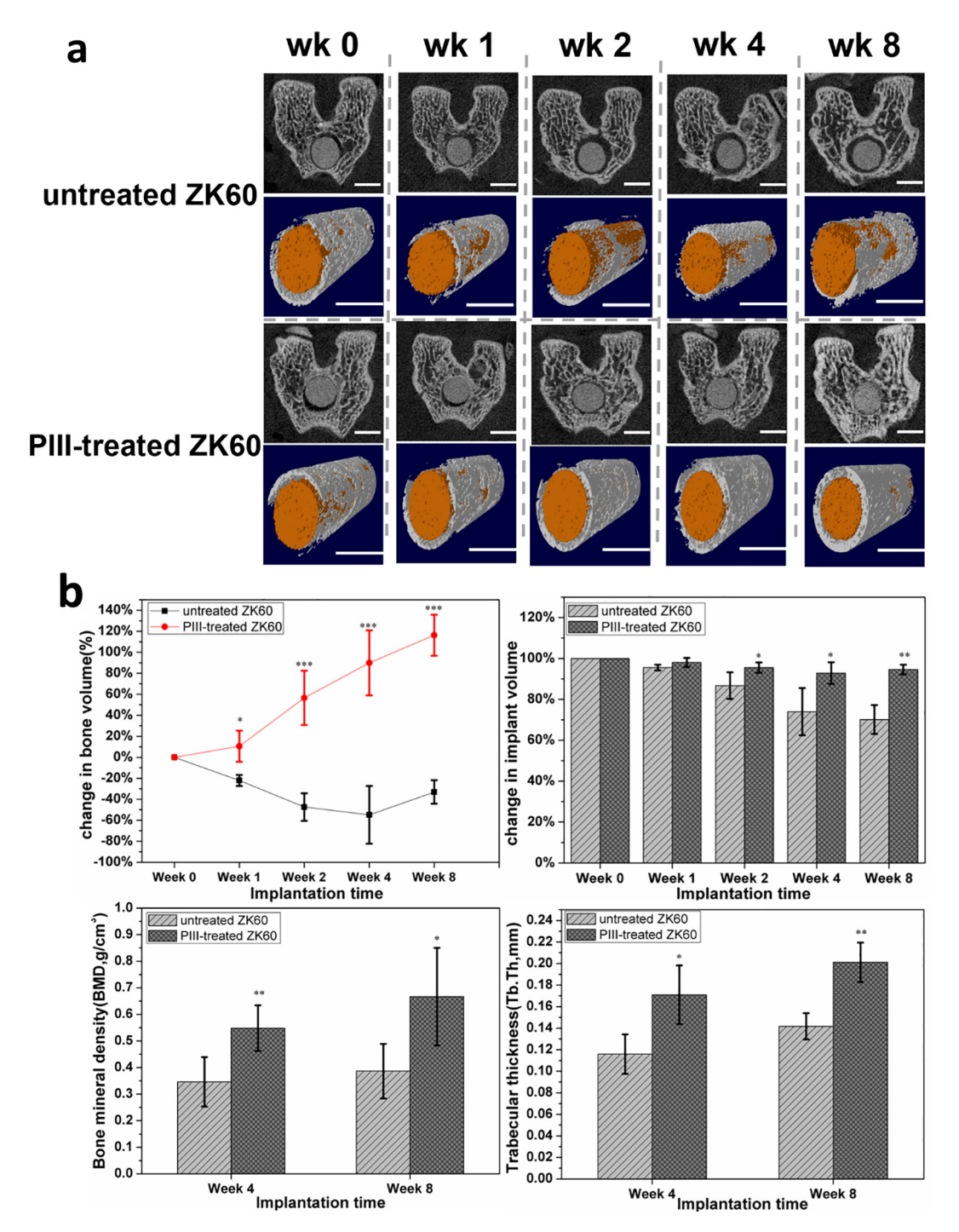


Fig. 8. Real-time Micro-CT evaluations of untreated and PIII treated ZK60 groups after post-surgery at various time points in rat intramedullary bone defect model. Fig. 8a referred to reconstruction images of the intercondylar fossa implanted with ZK60 rods and correspondent 3D reconstructed models at post-surgery 0, 1, 2, 4 and 8 weeks (scale bar: 2 mm). Fig. 8b exhibited change in new bone volume, change in implant volume, bone mineral density (BMD), and trabecular thickness (Tb, Th) of newly formed bone tissue in each group calculated by the CTAn software. *denotes the significant difference between untreated and PIII treated ZK60 groups (p < 0.05), **(p < 0.01), *** (p < 0.001).

moted corrosion resistance of magnesium substrates after plasma modification. More importantly, the absolute potential difference between E^{+} and E^{-} ($|E^{+}-E^{-}|$) of PIII-treated ZK60 (0.01 V in SBF; 0.04 V in DMEM) was significantly lower than that of the untreated sample (0.19 V in SBF; 0.1 V in DMEM), revealing that a retarded corrosion rate was achieved in the PIII-treated group due to the narrow potential difference. With regards to EIS spectra, $R_{\rm s}$ value

exhibits little difference between the untreated and PIII treated groups while the PIII treated ZK60 sample presents 9-fold and 33-fold increase of $R_{\rm f}$ and $R_{\rm t}$ respectively compared to the untreated sample in SBF solution. Similarly, 4-fold and 9-fold enhancement of $R_{\rm f}$ and $R_{\rm t}$ are also achieved in the DMEM solution. Values of CPE $_{\rm f}$ or CPE $_{\rm d1}$ depend on the admittance constant $Y_{\rm of}$ (or $Y_{\rm od1}$) and the indices of dispersion effects $n_{\rm f}$ (or $n_{\rm d1}$). $Y_{\rm of}$ and $Y_{\rm od1}$ in

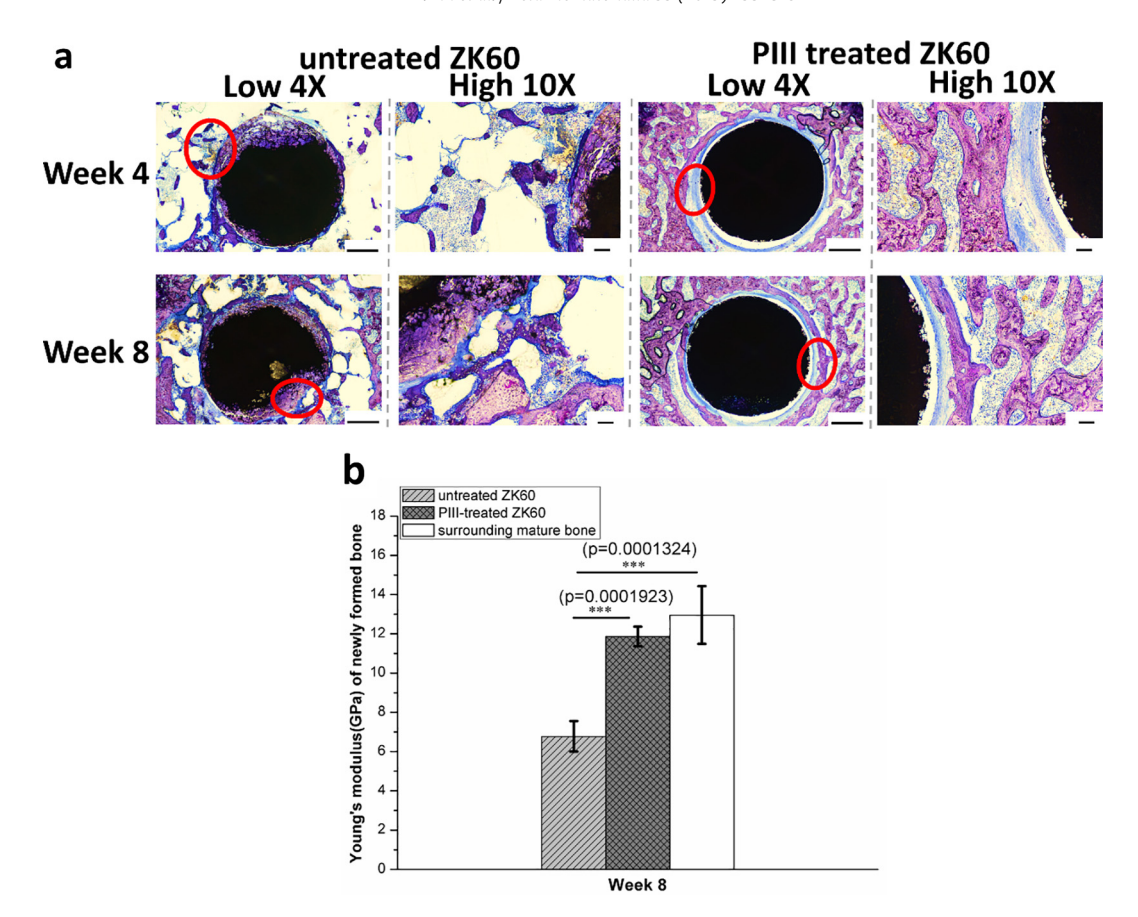


Fig. 9. Histological images and Young's modulus of new bone formation around the untreated and PIII treated ZK60 implants after post-surgery eight weeks. Fig. 9a showed Giemsa-stained images of newly formed bone tissues of each group cut from the cross section of femur (scale bar: $4X 500 \mu m$; $10 \times 100 \mu m$). The black and pink color stood for the implant and newly formed bony tissue respectively while the blue dotes referred to osteoclasts. The PIII treated group exhibited plenty of new bone tissue formed around the implant. Meanwhile, the bony tissue integrated closely with the implant. For the untreated group, much amount of bone had been resorbed during degradation of ZK60 implant and large numbers of osteoclasts were extremely active for bone resorption. Fig. 9b exhibited relative indentation modulus of newly formed bone tissues in each group (normalized to surrounding mature bone) at week 8. ***denotes the significant difference between untreated ZK60 and PIII treated ZK60 groups and difference between surrounding mature bone group and untreated ZK60 group (p < 0.001). (For interpretation of the references to color in this figure legend, the reader is referred to the web version of this article.)

the PIII treated sample are approximately10-fold and 10^4 -fold decrease than that of untreated sample after SBF immersion respectively. Since Values of CPE_f or CPE_{d1} are proportional to Y_{of} (or Y_{od1}), decreased Y_{of} and Y_{od1} in the PIII treated group equals to smaller CPE_f or CPE_{d1} which contributes to excellent anticorrosion property [58–60]. Furthermore, larger R_f and R_t indicate a more compacted protective layer on the sample surface which functions as strong barrier against dissolution of ZK60 substrates. Song et al [61,62] has already elucidated the corrosion mechanism of Mg substrates in corrosive solutions. Specifically, When ZK60 substrates are exposed to corrosive solutions, the second phase (intermetallic compound) is being the anodic electrode which dissolve Mg substrates into Mg^{2+} while Mg substrates occur cathodic reaction and produce hydrogen gas leading to local alkaline conditions:

$$Mg(s) \rightarrow Mg^{2+}(aq) + 2e^{-}$$
 (anodic reaction) (1)

$$2H_2O + 2e^- \rightarrow H_2 + 2OH^-(aq) \ (cathodic \ reaction) \eqno(2)$$

The $Mg(OH)_2$ layer is formed in the corrosive regions due to favorable local alkaline environment by the following overall reaction:

$$Mg(s) + 2H_2O \rightarrow H_2 + Mg(OH)_2(S)$$
 (3)

The deposited $Mg(OH)_2$ layer is easy to be dissolved and cannot protect corrosive attack since the SBF solution contains abundant chloride ions and the insoluble $Mg(OH)_2$ layer tends to transform into soluble $MgCl_2$:

$$Mg(OH)_2(S) + 2Cl^- \rightarrow MgCl_2(aq) + 2OH^-(aq) \tag{4}$$

Therefore, smaller R_f and R_t of untreated ZK60 sample attribute to native Mg(OH)₂ poor-protective layer formed on the surface. In contrary, after Ti and O PIII, a TiO₂ based nanolayer (main components: TiO₂ and MgO) effectively resists mass transportation and thereby makes chloride ions difficult to penetrate the ZK60 substrates. Hence, the TiO₂ based nanolayer acts as a strong barrier against corrosive solutions including chloride ions and remarkably retards ZK60 substrate dissolution.

4.2. Biocompatibility of PIII-treated ZK60 implant in vitro and vivo

The PIII treated ZK60 group exhibits enhanced osteoblastic activity *in vitro* and excellent osteoconductivity in the rat intramedullary bone defect model owing to modulation of magnesium ion delivery in the local microenvironment. Plenty of literatures has demonstrated that magnesium ions are beneficial to osteogenesis by promoting osteoblastic activity and/or inhibiting osteoclastic

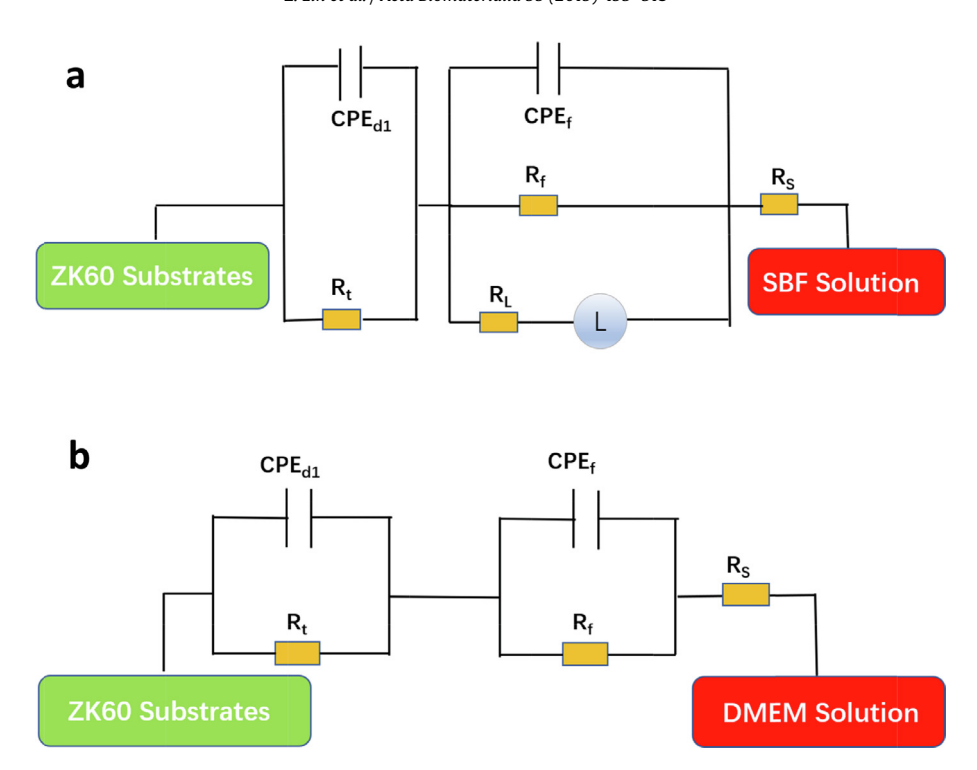


Fig. 10. Correspondent simulated equivalent circuit of EIS spectra of untreated and PIII treated ZK60 samples in the SBF and DMEM solutions at 37 °C.

activity [63]. Through activation of Notch signaling pathways by penetration into the TRPM7 channel [64,65], Mg ions can proliferate mesenchymal stem cells (MSCs). Meanwhile, Mg ions promote MSCs differentiation into osteoblasts by up-regulation of osteogenic expression of Col I, ALP and OPN [66,67]. However, high concentration of Mg ions has been reported to suppress human osteoblasts differentiation in vitro and may disorder the bone mineralization process by occupying the calcium-related signaling pathways [64]. Moreover, high level of extracellular Mg ions tends to inhibit the TRPM7 expression induced by other metallic ions (Ca, Zn, Mn and Co etc.) and alter intracellular balance of cation ions [68]. Hence, regulation of Mg ion release in vivo is a paramount issue for bone regeneration. In addition, due to the loss of magnesium through urination, sweating and excretion into gut, a normal adult has to absorb at least 100 mg/day in order to maintain the magnesium balance inside the body [69]. Therefore, the recommended average intake of magnesium for an adult is about 300-400 mg/day [70]. Based on the results of immersion tests, PIII-treated ZK60 sample maintains the release of Mg²⁺ at 50-100 ppm per day in SBF solution in which the magnesium release rate should be under the recommended level for daily intake. Moreover, our previous studies revealed that 50-200 ppm/day extracellular Mg ion could facilitate osteoblastic proliferation and differentiation in vitro and stimulate in-situ bone regeneration in vivo [33,71]. Hence, in vitro cell study, with satisfactory Mg ion delivery from the PIII treated group, MC3T3-E1 pre-osteoblasts present enhanced adhesion on the sample surface with spreading cytoskeleton and F-actin. Additionally, viability, proliferation and differentiation of MC3T3-E1pre-osteoblasts are apparently elevated 40%, 250% and 83% respectively when the cells were cocultured with PIII treated samples. Furthermore, osteogenic expressions of Type I Col I, OPN, ALP and RUNX2 are appreciably up-regulated as well via regulated Mg ion release in local microenvironment. Since more pre-osteoblasts favor to differentiation into osteoblasts by Mg ion stimulus, the bone remolding and healing process will be accelerated. In the rat intramedullary bone defect model, the PIII treated group begins to form the new bone around the implant only after post-surgery one week and the new bone volume achieves 116.3% growth at post-operation eight weeks. In addition, new bone qualities including BMD and trabecular thickness in the PIII treated group are significantly higher than that of the untreated group. The results of histological analysis and nano-indentation assay reveal that large amount of newly formed bony tissue in the PIII treated group is well mineralized and the mechanical property can almost reach the level of surrounding mature bone. All the promising results of newly formed bone in the PIII treated group attribute to modulation of Mg ion delivery in the local tissue microenvironment by the specific TiO₂/MgO nanolayer.

4.3. Antimicrobial activity of functionalized TiO₂/MgO nanolayer

As we all know, infection of orthopedic implants is the major reason for host immune rejection and implant failure since if bacteria are well attached to the surface of implants and it's quite difficult to inhibit their growth [72]. Therefore, prevention of bacteria infection is also a challenge for implant surgery. For magnesiumbased implant, some literatures have pointed out magnesium alloys can prevent biofilm formation of Pseudomonas sp and Staphylococcus aureu by the combined effects of high pH and high concentration of Mg ions [73,74]. However, most of reports are apt to believe that bacteria killing of magnesium alloys are ascribed from alkalinity (high pH level) caused by their degradation [75-77]. Although the elevated pH level (from 9 to 11) during degradation of magnesium-based alloys can inhibit bacteria growth, this alkalosis microenvironment is also detrimental to survival and proliferation of osteoblasts and MSCs. Consequently, if magnesium-based implants are applied in orthopedics, it should possess antibacterial property and great cyto-compatibility in vivo. The results of antimicrobial assays against S. aureus show that the PIII treated

Corrosion current density and corrosion potentials of forward scan ((†corr,E*) and reverse scan ((jcorr,E*) of untreated and PIII treated ZK60 samples obtained from the cyclic polarization curves and the fitted EIS data calculated from

correspond	orrespondent equivalent enemit.											
Solution	Sample	i ⁺ _{corr} (A/cm ²)		E ⁺ (V/SCE)	E-(V/SCE)	Rs(Ωcm²)	$\begin{array}{cccc} E^{\cdot}(V/SCE) & Rs(\Omega cm^2) & Y_{0f}\left(\Omega^{-1} \ cm^{-2} & n_f \\ & s^{-n} \end{array} \label{eq:energy}$	nr	R_{f} or $R_{pore}(\Omega cm^{2})$	$\begin{array}{cc} Y_{0d1}(\Omega^{-1}\ cm^{-2} & n_{dl} \\ s^{-n}) \end{array}$	n _{dl}	Rt(Ωcm²)
SBF	untreated ZK60	5.57E- 05 ± 1.21E-06	3.19E- 04 ± 1.85E-05	-1.52 ± 0.03	-1.71 ± 0.02	17.65 ± 0.08	3.00E-05 ± 1.2E-	-1.52 ± 0.03 -1.71 ± 0.02 17.65 ± 0.08 $3.00E-05 \pm 1.2E 0.8848 \pm 0.0013$ 44.24 ± 0.14	44.24 ± 0.14	1.72E-02 ± 1.7E-	1.72E-02 ± 1.7E- 0.3442 ± 0.0015 18.16 ± 0.17 03	18.16 ± 0.17
	PIII-treated ZK60	6.38E- 06±2.71E-07	1.06E- 05 ± 3.13E-06	-1.43 ± 0.02	-1.42 ± 0.01	-1.43 ± 0.02 -1.42 ± 0.01 17.61 ± 0.13 3.265 0.04 ± 2.7	3.26E- 04 ± 2.75E-05	0.6983 ± 0.0024 397.6 ± 0.23	397.6 ± 0.23	1.73E-06 ± 8.1E- 07	0.9035 ± 0.0021 598.3 ± 0.71	598.3 ± 0.71
DMEM	untreated ZK60	7.70E- 06 ± 2.36E-07	2.00E- 04 ± 3.24E-05	-1.37 ± 0.02	-1.47 ± 0.01	-1.37 ± 0.02 -1.47 ± 0.01 21.94 ± 0.09 $1.32E-0.03 \pm 3.7$	1.32E- 03 ± 3.16E-04	0.4281 ± 0.0031 326.6 ± 0.34	326.6 ± 0.34	2.55E- 05 ± 3.22E-06	0.9211 ± 0.0037 124.2 ± 0.48	124.2 ± 0.48
	PIII-treated ZK60	2.91E- 06 ± 1.36E-07		-1.41 ± 0.01	-1.37 ± 0.03	-1.41 ± 0.01 -1.37 ± 0.03 21.22 ± 0.05 $3.54E$ - 06 ± 2.8	3.54E- 06 ± 2.88E-07	0.8454 ± 0.0017 1343 ± 2.31	1343 ± 2.31	1.27E- 06 ± 3.46E-07	0.7595 ± 0.0019 1107 ± 4.32	1107 ± 4.32

ZK60 samples irradiated by UV light can effectively kill 99.31% bacteria on the surface after 6 h incubation while untreated samples only inhibit 62.32% growth of *S. aureus*. For the untreated groups, bacteria disinfection stems from the elevated pH level caused by rapid corrosion of ZK60 substrates as the pH of bacteria suspension increases to 9.7 and 10.0 respectively after incubation for 6 and 12 h. Moreover, during the corrosion process of Mg substrates, Mg(OH)₂ precipitates are deposited on the surface, which has been reported to prevent bacteria adhesion to some extent [78,79]. However, the alkalosis microenvironment induced by degradation of untreated ZK60 samples jeopardizes the mineralization process of bone, as shown in Fig. 9. On the other hand, antibacterial property of the PIII treated ZK60 groups mainly attributes to large amount of ROS generation induced by photocatalytic disinfection activity of TiO₂-based nanolayer rather than elevated pH level. Nevertheless, overproduction of reactive oxygen species may result in potential adverse effects on osteogenesis that causes the disruption of cellular oxidant/antioxidant balance and therefore disorders the bone tissue healing process [80]. A study revealed that bone-implant integration of titanium implant can be enhanced through inhibition of reactive oxygen species overproduction via the PI3K-Akt pathway [81]. Furthermore, the oxidative stress interferes the bone mineralization process resulting from the downregulation of vascular endothelial growth factor (VEGF) and therefore the cell cycle, differentiation and apoptosis of mesenchymal stromal cells (MSCs) are arrested [82]. Consequently, an appropriate amount of reactive oxygen species generated under UV irradiation is able to regulate antibacterial activity, while maintaining the bone regeneration ability of magnesium substrates. The antibacterial mechanism of TiO₂ nano-particles or films irradiated by UV light has been extensively investigated [83-85]. Specifically, as shown in Fig. 11, under UV (<390 nm) irradiation, the TiO₂-based nanolayer is subjected to charge separation, leading to generation of positive charged holes (h_v) on the valence band and electrons (e_c^-) on the conduction band. Then, the positive charged holes easily occur oxidative reaction, which attracts electrons from water or hydroxyl ions to generate hydroxyl radicals (,OH). Meanwhile, electrons tend to reduce molecular oxygen to form the superoxide radical (O_2^-) . The singlet oxygen $(^1O_2)$ can be produced indirectly via superoxide from the O_2^- . Through recombination between h_v⁺/e_c pairs, endless amount of ROS (containing O_2^- , OH and O_2) can be generated under UV irradiation. Furthermore, the three kinds of ROS penetrate into the cell wall of S. aureus and involve in lipid peroxidation of bacteria membranes, resulting in oxidation of nucleolus, amino acids and DNA strand breakages [86].

5. Conclusions

In this paper, we have constructed a TiO₂/MgO nanolayer by Ti and O dual PIII technique to suppress rapid corrosion of ZK60 Mg substrates, improve biocompatibility in vitro and vivo with controlled release of magnesium ion and enhance antimicrobial properties. In the rat intramedullary bone defect model, the elevated new bone volume, bone mineral density and trabecular thickness are observed in the PIII treated group while the implant volume of PIII treated ZK60 can still retain 94%. Additionally, the Giemsastaining results show that the newly form bony tissue around the PIII treated implant exhibits well mineralized structure and its mechanical property can almost achieve the level of surrounding mature bone. Surprisingly, the PIII treated ZK60 sample under UV irradiation can effectively kill 98.63% and 99.31% S. aureus on the surface after 6 and 12 h incubation. The antimicrobial mechanism of PIII treated ZK60 is ascribed to the extracellular reactive oxygen species (ROS) produced by the nano-layer. To sum up,

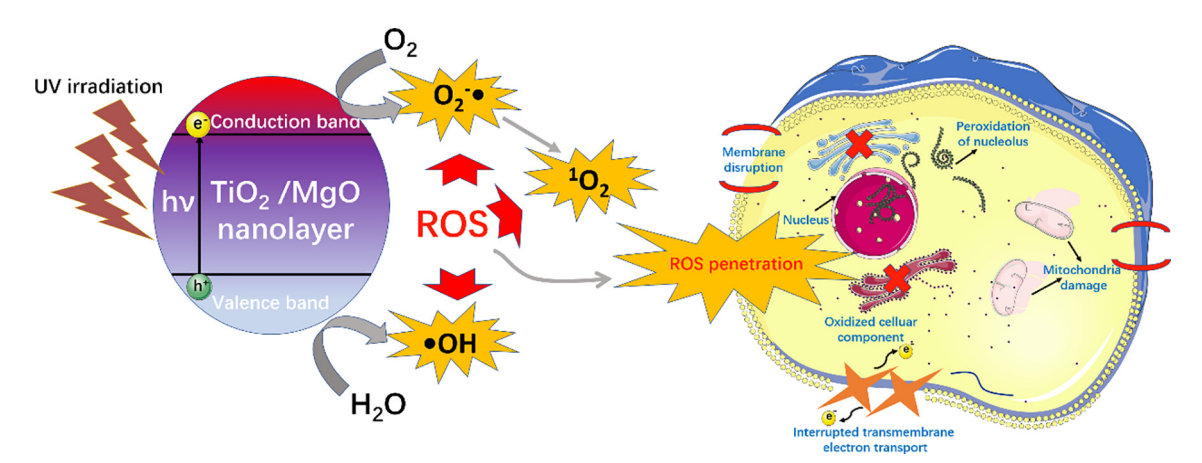


Fig. 11. The mechanism diagram of antimicrobial property of PIII treated ZK60 under UV irradiation. The antimicrobial mechanism mainly involved ROS generation of hydroxyl radicals (.OH), superoxide radical (O_2^-) and singlet oxygen (1O_2) induced by TiO₂/MgO nanolayer under UV light stimulation, which could penetrate into the bacteria membrane and lead to peroxidation of nucleolus, DNA strand breakages, mitochondria damage and membrane disruption.

the multifunctional TiO₂/MgO nanolayer by PIII technique makes magnesium implants promising candidate for orthopaedic applications.

Acknowledgements

This work was financially supported by the China Postdoctoral Science Foundation (2019M653060), General Research Fund of Hong Kong Research Grant Council (#17214516), National Natural Science Foundation-Research Grant Council (N_HKU725-16), Seed Fund for Translational and Applied Research (HKU, 201611160006), Sanming Project of Medicine in Shenzhen "Team of Excellence in Spinal Deformities and Spinal Degeneration Disease" (SZSM201612055), National Natural Science Foundation of China (31370957 & 81572113) and Shenzhen Science and Technology Funding (JCYJ20160429190821781, JCYJ20160429185449249 & JCYJ20160608153641020) and Guangdong Scientific Plan (2014A030313743), and the Science and Technology Commission of Shanghai Municipality (18410760600) and International Partnership Program of Chinese Academy of Sciences (GJHZ1850).

Competing interests

The authors declare no competing financial interests.

Appendix A. Supplementary data

Supplementary data to this article can be found online at https://doi.org/10.1016/j.actbio.2019.09.008.

References

- [1] M. Kaur, K. Singh, Review on titanium and titanium based alloys as biomaterials for orthopaedic applications, Mater. Sci. Eng., C (2019).
- [2] D. Zhang, Z. Qi, H. Shen, B. Wei, Y. Zhang, Z. Wang, In vitro degradation and cytocompatibility of magnesium alloy coated with Hf/PLLA duplex coating, Mater. Lett. 213 (2018) 249–252.
- [3] W. Xu, N. Birbilis, G. Sha, Y. Wang, J.E. Daniels, Y. Xiao, M. Ferry, A high-specific-strength and corrosion-resistant magnesium alloy, Nat. Mater. 14 (2015) 1229–1235.
- [4] F. Witte, Reprint of: The history of biodegradable magnesium implants: A review, Acta Biomater. 23 (2015) S28–S40.
- [5] W. Wang, K.W. Yeung, Bone grafts and biomaterials substitutes for bone defect repair: A review, Bioact. Mater. 2 (2017) 224–247.
- [6] D. Zhao, F. Witte, F. Lu, J. Wang, J. Li, L. Qin, Current status on clinical applications of magnesium-based orthopaedic implants: A review from clinical translational perspective, Biomaterials 112 (2017) 287–302.

- [7] J. Yang, G.L. Koons, G. Cheng, L. Zhao, A.G. Mikos, F.-Z. Cui, A review on the exploitation of biodegradable magnesium-based composites for medical applications, Biomed. Mater. (2017).
- [8] M. Shimaya, T. Muneta, S. Ichinose, K. Tsuji, I. Sekiya, Magnesium enhances adherence and cartilage formation of synovial mesenchymal stem cells through integrins, Osteoarthritis Cartilage 18 (2010) 1300–1309.
- [9] S. Won, Y.-H. Huh, L.-R. Cho, H.-S. Lee, E.-S. Byon, C.-J. Park, Cellular response of human bone marrow derived mesenchymal stem cells to titanium surfaces implanted with calcium and magnesium ions, Tissue Eng. Regener. Med. 14 (2017) 123–131.
- [10] R.W. Li, N.T. Kirkland, J. Truong, J. Wang, P.N. Smith, N. Birbilis, D.R. Nisbet, The influence of biodegradable magnesium alloys on the osteogenic differentiation of human mesenchymal stem cells, J. Biomed. Mater. Res. Part A 102 (2014) 4346–4357.
- [11] G.L. Song, A. Atrens, Corrosion mechanisms of magnesium alloys, Adv. Eng. Mater. 1 (1999) 11–33.
- [12] G. Song, Control of biodegradation of biocompatable magnesium alloys, Corros. Sci. 49 (2007) 1696–1701.
- [13] N. Hort, Y. Huang, D. Fechner, M. Störmer, C. Blawert, F. Witte, C. Vogt, H. Drücker, R. Willumeit, K. Kainer, Magnesium alloys as implant materials-principles of property design for Mg-RE alloys, Acta Biomater. 6 (2010) 1714–1725.
- [14] F. Witte, V. Kaese, H. Haferkamp, E. Switzer, A. Meyer-Lindenberg, C. Wirth, H. Windhagen, In vivo corrosion of four magnesium alloys and the associated bone response, Biomaterials 26 (2005) 3557–3563.
- [15] F. Witte, J. Fischer, J. Nellesen, H.-A. Crostack, V. Kaese, A. Pisch, F. Beckmann, H. Windhagen, In vitro and in vivo corrosion measurements of magnesium alloys, Biomaterials 27 (2006) 1013–1018.
- [16] P. Amaravathy, T. Sampath Kumar, Novel strontium doped zinc calcium phosphate conversion coating on AZ31 magnesium alloy for biomedical applications, J. Biomimetics Biomater. Biomed. Eng. Trans. Tech. Publ. (2017) 57, 67
- [17] H. Tang, Y. Han, T. Wu, W. Tao, X. Jian, Y. Wu, F. Xu, Synthesis and properties of hydroxyapatite-containing coating on AZ31 magnesium alloy by micro-arc oxidation, Appl. Surf. Sci. 400 (2017) 391–404.
- [18] Y. Reyes, A. Durán, Y. Castro, Glass-like cerium sol-gel coatings on AZ31B magnesium alloy for controlling the biodegradation of temporary implants, Surf. Coat. Technol. 307 (2016) 574–582.
- [19] M. Mhaede, F. Pastorek, B. Hadzima, Influence of shot peening on corrosion properties of biocompatible magnesium alloy AZ31 coated by dicalcium phosphate dihydrate (DCPD), Mater. Sci. Eng., C 39 (2014) 330–335.
 [20] P. Xiong, J. Yan, P. Wang, Z. Jia, W. Zhou, W. Yuan, Y. Li, Y. Liu, Y. Cheng, D.
- [20] P. Xiong, J. Yan, P. Wang, Z. Jia, W. Zhou, W. Yuan, Y. Li, Y. Liu, Y. Cheng, D. Chen, A pH-sensitive self-healing coating for biodegradable magnesium implants, Acta Biomater. (2019).
- [21] T. Kraus, S. Fischerauer, S. Treichler, E. Martinelli, J. Eichler, A. Myrissa, S. Zötsch, P.J. Uggowitzer, J.F. Löffler, A.M. Weinberg, The influence of biodegradable magnesium implants on the growth plate, Acta Biomater. 66 (2018) 109–117.
- [22] K.-H. Cheon, C. Gao, M.-H. Kang, H.-D. Jung, T.-S. Jang, H.-E. Kim, Y. Li, J. Song, A crack-free anti-corrosive coating strategy for magnesium implants under deformation, Corros. Sci. 132 (2018) 116–124.
- [23] G. Li, L. Zhang, L. Wang, G. Yuan, K. Dai, J. Pei, Y. Hao, Dual modulation of bone formation and resorption with zoledronic acid-loaded biodegradable magnesium alloy implants improves osteoporotic fracture healing: An in vitro and in vivo study, Acta Biomater. 65 (2018) 486–500.
- [24] Chu PK. Modification of Biomaterials and Biomedical Devices by Plasma Immersion Ion Implantation & Deposition and Related Techniques. Ion Implantation Technology (IIT), 2016 21st International Conference on: IEEE; 2016. p. 1-5.

- [25] P.K. Chu, J. Chen, L. Wang, N. Huang, Plasma-surface modification of biomaterials, Mater. Sci. Eng. R: Rep. 36 (2002) 143–206.
- [26] M.I. Jamesh, G. Wu, Y. Zhao, D.R. McKenzie, M.M. Bilek, P.K. Chu, Effects of zirconium and oxygen plasma ion implantation on the corrosion behavior of ZK60 Mg alloy in simulated body fluids, Corros. Sci. 82 (2014) 7–26.
- [27] M.I. Jamesh, G. Wu, Y. Zhao, W. Jin, D.R. McKenzie, M.M. Bilek, P.K. Chu, Effects of zirconium and nitrogen plasma immersion ion implantation on the electrochemical corrosion behavior of Mg-Y-RE alloy in simulated body fluid and cell culture medium, Corros. Sci. 86 (2014) 239-251.
- [28] Y. Zhao, M.I. Jamesh, W.K. Li, G. Wu, C. Wang, Y. Zheng, K.W. Yeung, P.K. Chu, Enhanced antimicrobial properties, cytocompatibility, and corrosion resistance of plasma-modified biodegradable magnesium alloys, Acta Biomater. 10 (2014) 544–556.
- [29] L. Cao, X. Wu, Q. Wang, J. Wang, Biocompatible nanocomposite of TiO2 incorporated bi-polymer for articular cartilage tissue regeneration: A facile material, J. Photochem. Photobiol., B 178 (2018) 440–446.
- [30] A. Aldaadaa, M. Al Qaysi, G. Georgiou, M.A. Leeson R, J.C. Knowles, Physical properties and biocompatibility effects of doping SiO2 and TiO2 into phosphate-based glass for bone tissue engineering, J. Biomater. Appl. 33 (2018) 271–280.
- [31] K. Ramos-Corella, M. Sotelo-Lerma, A. Gil-Salido, J. Rubio-Pino, O. Auciello, M. Quevedo-López, Controlling crystalline phase of TiO2 thin films to evaluate its biocompatibility, Mater. Technol. (2019) 1–8.
- [32] J. Raphel, M. Holodniy, S.B. Goodman, S.C. Heilshorn, Multifunctional coatings to simultaneously promote osseointegration and prevent infection of orthopaedic implants, Biomaterials 84 (2016) 301–314.
- [33] Z. Lin, J. Wu, W. Qiao, Y. Zhao, K.H. Wong, P.K. Chu, L. Bian, S. Wu, Y. Zheng, K. M. Cheung, Precisely controlled delivery of magnesium ions thru sponge-like monodisperse PLGA/nano-MgO-alginate core-shell microsphere device to enable in-situ bone regeneration, Biomaterials 174 (2018) 1–16.
- [34] X. Chen, X. Huang, C. Zheng, Y. Liu, T. Xu, J. Liu, Preparation of different sized nano-silver loaded on functionalized graphene oxide with highly effective antibacterial properties, J. Mater. Chem. B 3 (2015) 7020–7029.
- [35] H.M. Wong, Y. Zhao, F.K. Leung, T. Xi, Z. Zhang, Y. Zheng, S. Wu, K.D. Luk, K. Cheung, P.K. Chu, Functionalized polymeric membrane with enhanced mechanical and biological properties to control the degradation of magnesium alloy, Adv. Healthcare Mater. 6 (2017).
- [36] W. Li, D. Li, Influence of surface morphology on corrosion and electronic behavior, Acta Mater. 54 (2006) 445–452.
- [37] J.F. Dyet, W.G. Watts, D.F. Ettles, A.A. Nicholson, Mechanical properties of metallic stents: how do these properties influence the choice of stent for specific lesions?, Cardiovasc Intervent. Radiol. 23 (2000) 47–54.
- [38] D.O. Costa, B.A. Allo, R. Klassen, J.L. Hutter, S.J. Dixon, A.S. Rizkalla, Control of surface topography in biomimetic calcium phosphate coatings, Langmuir 28 (2012) 3871–3880.
- [39] M. Järn, S. Areva, V. Pore, J. Peltonen, M. Linden, Topography and surface energy dependent calcium phosphate formation on sol—gel derived TiO2 coatings, Langmuir 22 (2006) 8209–8213.
- [40] B.C. Ward, T.J. Webster, The effect of nanotopography on calcium and phosphorus deposition on metallic materials in vitro, Biomaterials 27 (2006) 3064–3074.
- [41] S. Lossdörfer, Z. Schwartz, L. Wang, C. Lohmann, J. Turner, M. Wieland, D.L. Cochran, B. Boyan, Microrough implant surface topographies increase osteogenesis by reducing osteoclast formation and activity, J. Biomed. Mater. Res. Part A 70 (2004) 361–369.
- [42] E.J. Kim, C.A. Boehm, A. Mata, A.J. Fleischman, G.F. Muschler, S. Roy, Post microtextures accelerate cell proliferation and osteogenesis, Acta Biomater. 6 (2010) 160–169.
- [43] H. Zreiqat, C. Howlett, A. Zannettino, P. Evans, G. Schulze-Tanzil, C. Knabe, M. Shakibaei, Mechanisms of magnesium-stimulated adhesion of osteoblastic cells to commonly used orthopaedic implants, J. Biomed. Mater. Res. 62 (2002) 175–184
- [44] Y. Yamasaki, Y. Yoshida, M. Okazaki, A. Shimazu, T. Uchida, T. Kubo, Y. Akagawa, Y. Hamada, J. Takahashi, N. Matsuura, Synthesis of functionally graded MgCO3 apatite accelerating osteoblast adhesion, J. Biomed. Mater. Res. 62 (2002) 99–105.
- [45] K. Zhang, S. Lin, Q. Feng, C. Dong, Y. Yang, G. Li, L. Bian, Nanocomposite hydrogels stabilized by self-assembled multivalent bisphosphonate-magnesium nanoparticles mediate sustained release of magnesium ion and promote in-situ bone regeneration, Acta Biomater. 64 (2017) 389–400.
- [46] Z. Yuan, P. Wei, Y. Huang, W. Zhang, F. Chen, X. Zhang, J. Mao, D. Chen, Q. Cai, X. Yang, Injectable PLGA microspheres with tunable magnesium ion release for promoting bone regeneration, Acta Biomater. 85 (2019) 294–309.
- [47] L. Mao, G. Yuan, S. Wang, J. Niu, G. Wu, W. Ding, A novel biodegradable Mg-Nd-Zn-Zr alloy with uniform corrosion behavior in artificial plasma, Mater. Lett. 88 (2012) 1-4.
- [48] L. Mao, L. Shen, J. Niu, J. Zhang, W. Ding, Y. Wu, R. Fan, G. Yuan, Nanophasic biodegradation enhances the durability and biocompatibility of magnesium alloys for the next-generation vascular stents, Nanoscale 5 (2013) 9517–9522.
- [49] W. Jin, G. Wu, H. Feng, W. Wang, X. Zhang, P.K. Chu, Improvement of corrosion resistance and biocompatibility of rare-earth WE43 magnesium alloy by neodymium self-ion implantation, Corros. Sci. 94 (2015) 142–155.
- [50] C. Liu, Y. Wang, R. Zeng, X. Zhang, W. Huang, P. Chu, In vitro corrosion degradation behaviour of Mg–Ca alloy in the presence of albumin, Corros. Sci. 52 (2010) 3341–3347.

- [51] Y. Shen, W. Liu, K. Lin, H. Pan, B.W. Darvell, S. Peng, C. Wen, L. Deng, W.W. Lu, J. Chang, Interfacial pH: a critical factor for osteoporotic bone regeneration, Langmuir 27 (2011) 2701–2708.
- [52] J. Ma, N. Zhao, L. Betts, D. Zhu, Bio-adaption between magnesium alloy stent and the blood vessel: a review, J. Mater. Sci. Technol. 32 (2016) 815–826.
- [53] C. Janning, E. Willbold, C. Vogt, J. Nellesen, A. Meyer-Lindenberg, H. Windhagen, F. Thorey, F. Witte, Magnesium hydroxide temporarily enhancing osteoblast activity and decreasing the osteoclast number in perimplant bone remodelling, Acta Biomater. 6 (2010) 1861–1868.
- [54] M. Leidi, F. Dellera, M. Mariotti, J.A. Maier, High magnesium inhibits human osteoblast differentiation in vitro, Magnes. Res. 24 (2011) 1–6.
- [55] H.M. Wong, K.W. Yeung, K.O. Lam, V. Tam, P.K. Chu, K.D. Luk, K.M. Cheung, A biodegradable polymer-based coating to control the performance of magnesium alloy orthopaedic implants, Biomaterials 31 (2010) 2084–2096.
- [56] R.A. Lindtner, C. Castellani, S. Tangi, G. Zanoni, P. Hausbrandt, E.K. Tschegg, S.E. Stanzl-Tschegg, A.-M. Weinberg, Comparative biomechanical and radiological characterization of osseointegration of a biodegradable magnesium alloy pin and a copolymeric control for osteosynthesis, J. Mech. Behav. Biomed. Mater. 28 (2013) 232–243.
- [57] C. Liu, Y. Xin, X. Tian, P.K. Chu, Corrosion behavior of AZ91 magnesium alloy treated by plasma immersion ion implantation and deposition in artificial physiological fluids, Thin Solid Films 516 (2007) 422–427.
- [58] M.-J. Wang, C.-F. Li, S.-K. Yen, Electrolytic MgO/ZrO 2 duplex-layer coating on AZ91D magnesium alloy for corrosion resistance, Corros. Sci. 76 (2013) 142– 153
- [59] G.-L. Song, Z. Shi, Corrosion mechanism and evaluation of anodized magnesium alloys, Corros. Sci. 85 (2014) 126–140.
- [60] M. Morad, Inhibition of iron corrosion in acid solutions by Cefatrexyl: Behaviour near and at the corrosion potential, Corros. Sci. 50 (2008) 436–448.
- [61] G. Song, A. Atrens, Understanding magnesium corrosion—a framework for improved alloy performance, Adv. Eng. Mater. 5 (2003) 837–858.
- [62] F. Cao, Z. Shi, G.-L. Song, M. Liu, M.S. Dargusch, A. Atrens, Stress corrosion cracking of several solution heat-treated Mg-X alloys, Corros. Sci. 96 (2015) 121-132.
- [63] R.K. Rude, H.E. Gruber, Magnesium deficiency and osteoporosis: animal and human observations, J. Nutr. Biochem. 15 (2004) 710–716.
- [64] E. Abed, R. Moreau, Importance of melastatin-like transient receptor potential 7 and cations (magnesium, calcium) in human osteoblast-like cell proliferation, Cell Prolif. 40 (2007) 849–865.
- [65] J.M. Díaz-Tocados, C. Herencia, J.M. Martínez-Moreno, A.M. De Oca, M.E. Rodríguez-Ortiz, N. Vergara, A. Blanco, S. Steppan, Y. Almadén, M. Rodríguez, Magnesium chloride promotes osteogenesis through notch signaling activation and expansion of mesenchymal stem cells, Sci. Rep. 7 (2017) 7839.
- [66] C. Yang, G. Yuan, J. Zhang, Z. Tang, X. Zhang, K. Dai, Effects of magnesium alloys extracts on adult human bone marrow-derived stromal cell viability and osteogenic differentiation, Biomed. Mater. 5 (2010) 045005.
- [67] H. Sun, C. Wu, K. Dai, J. Chang, T. Tang, Proliferation and osteoblastic differentiation of human bone marrow-derived stromal cells on akermanitebioactive ceramics. Biomaterials 27 (2006) 5651–5657.
- [68] M.K. Monteilh-Zoller, M.C. Hermosura, M.J. Nadler, A.M. Scharenberg, R. Penner, A. Fleig, TRPM7 provides an ion channel mechanism for cellular entry of trace metal ions, J. Gen. Physiol. 121 (2003) 49–60.
- [69] J. Vormann, Magnesium: nutrition and metabolism, Mol. Aspects Med. 24 (2003) 27–37.
- [70] J. Vormann, M. Anke, Dietary magnesium: supply, requirements and recommendations-results from duplicate and balance studies in man, J. Clin. Basic Cardiol. 5 (2002) 49–53.
- [71] H.M. Wong, S. Wu, P.K. Chu, S.H. Cheng, K.D. Luk, K.M. Cheung, K.W. Yeung, Low-modulus Mg/PCL hybrid bone substitute for osteoporotic fracture fixation, Biomaterials 34 (2013) 7016–7032.
- [72] G.S. Chatzopoulos, L.F. Wolff, Implant failure and history of failed endodontic treatment: A retrospective case-control study, J. Clin. Exp. Dent. 9 (2017) e1322–e1328.
- [73] H. Feng, G. Wang, W. Jin, X. Zhang, Y. Huang, A. Gao, H. Wu, G. Wu, P.K. Chu, Systematic study of inherent antibacterial properties of magnesium-based biomaterials, ACS Appl. Mater. Interfaces 8 (2016) 9662–9673.
- [74] K. Nandakumar, K.R. Sreekumari, Y. Kikuchi, Antibacterial properties of magnesium alloy AZ31B: in-vitro studies using the biofilm-forming bacterium Pseudomonas sp, Biofouling 18 (2002) 129–135.
- [75] D.A. Robinson, R.W. Griffith, D. Shechtman, R.B. Evans, M.G. Conzemius, In vitro antibacterial properties of magnesium metal against Escherichia coli, Pseudomonas aeruginosa and Staphylococcus aureus, Acta Biomater. 6 (2010) 1869–1877.
- [76] Y. Li, G. Liu, Z. Zhai, L. Liu, H. Li, K. Yang, L. Tan, P. Wan, X. Liu, Z. Ouyang, Antibacterial properties of magnesium in vitro and in an in vivo model of implant-associated methicillin-resistant Staphylococcus aureus infection, Antimicrob. Agents Chemother. 58 (2014) 7586–7591.
- [77] J.Y. Lock, E. Wyatt, S. Upadhyayula, A. Whall, V. Nuñez, V.I. Vullev, H. Liu, Degradation and antibacterial properties of magnesium alloys in artificial urine for potential resorbable ureteral stent applications, J. Biomed. Mater. Res. Part A 102 (2014) 781–792.
- [78] Y.H. Leung, A. Ng, X. Xu, Z. Shen, L.A. Gethings, M.T. Wong, C. Chan, M.Y. Guo, Y. H. Ng, A.B. Djurišić, Mechanisms of antibacterial activity of MgO: non-ROS mediated toxicity of MgO nanoparticles towards Escherichia coli, Small 10 (2014) 1171–1183.

- [79] X. Pan, Y. Wang, Z. Chen, D. Pan, Y. Cheng, Z. Liu, Z. Lin, X. Guan, Investigation of antibacterial activity and related mechanism of a series of nano-Mg (OH) 2, ACS Appl. Mater. Interfaces 5 (2013) 1137–1142.
- [80] L. Wang, X. Zhao, B-y Wei, Y. Liu, X-y Ma, J. Wang, P-c Cao, Y. Zhang, Y-b Yan, W. Lei, Insulin improves osteogenesis of titanium implants under diabetic conditions by inhibiting reactive oxygen species overproduction via the PI3K-Akt pathway, Biochimie 108 (2015) 85–93.
- [81] M.M. Bekhite, A. Finkensieper, F.A. Abou-Zaid, I.K. El-Shourbagy, K.M. Omar, H.-R. Figulla, H. Sauer, M. Wartenberg, Static electromagnetic fields induce vasculogenesis and chondro-osteogenesis of mouse embryonic stem cells by reactive oxygen species-mediated up-regulation of vascular endothelial growth factor, Stem Cells Dev. 19 (2009) 731–743.
- [82] F. Atashi, A. Modarressi, M.S. Pepper, The role of reactive oxygen species in mesenchymal stem cell adipogenic and osteogenic differentiation: a review, Stem Cells Dev. 24 (2015) 1150–1163.
- [83] H.A. Foster, I.B. Ditta, S. Varghese, A. Steele, Photocatalytic disinfection using titanium dioxide: spectrum and mechanism of antimicrobial activity, Appl. Microbiol. Biotechnol. 90 (2011) 1847–1868.
- [84] D. Stoyanova, I. Ivanova, O. Angelov, T. Vladkova, Antibacterial activity of thin films TiO2 doped with Ag and Cu on Gracilicutes and Firmicutes bacteria, BioDiscovery 20 (2017) e21596.
- [85] A. Nazerah, A. Ismail, J. Jaafar. Incorporation of bactericidal nanomaterials in development of antibacterial membrane for biofouling mitigation: A mini review, 2017.
- [86] Y. Li, W. Zhang, J. Niu, Y. Chen, Mechanism of photogenerated reactive oxygen species and correlation with the antibacterial properties of engineered metaloxide nanoparticles, ACS Nano 6 (2012) 5164–5173.